

CHAPTER IV

Experimental Configuration

4.1 Magnetron Anodes: Smoothbore

The Michigan Electron Long Beam Accelerator-Ceramic insulator (MELBA-C), shown in Fig. 4.1, is an eight stage pulsed Marx bank composed of 16, 1 μF , capacitors (2 capacitors per stage) which may be charged up to ± 100 kV (typically ± 30 kV each). MELBA-C utilizes an Abramyan circuit to generate a flattop voltage waveform for durations of 200 to 1000 ns. The Abramyan circuit utilizes a low frequency LRC circuit to subtract the initial peak of the Marx bank discharge and then add to the decaying voltage waveform at a later point in time corresponding to a half period of the resonant LRC circuit [75]. The capacitors, as is typical for a Marx bank configuration, charge in parallel and discharge in series to cumulatively add the voltage from each capacitor. Seven of these stages (14 capacitors) are charged using the main Marx power supply, while the remaining stage (2 capacitors) is allocated to the Abramyan circuit and subsequently charged to the reverse polarity. MELBA-C is capable of delivering a -1 MV pulse for durations of up to 1000 ns if operated at peak charging values with negligible losses. Experimentation on the RPM at the University of Michigan uses MELBA-C to produce -300 kV pulsed voltages for durations of 200-700 ns [76].



Figure 4.1. Photograph of the interior of the Michigan Electron Long Beam Accelerator-Ceramic insulator (MELBA-C) Marx Bank.

The RPM experiments at the University of Michigan were conducted in three stages corresponding to alterations of the RPM anode structure which include the smooth-bore anode, RPM-12a, and RPM-12a with coaxial extraction. Each of these stages are broken down by the type of cathode used during each experiment. The smooth-bore RPM anode shown in Fig. 4.2A was composed of 0.32 cm thick sheet-copper and featured a planar regime which extends 20 cm in the transverse direction and was bounded by 10.15 cm diameter cylindrical bends on either end to form a continuous structure.

The smoothbore anode, primarily used to experimentally validate Hull cutoff estimates and scale current emission, was operated with the first solid cathode prototype (SC-1) as well as a low current variant of the solid cathode (LC-1). Time resolved voltage and entrance current measurements were made using a copper sulfate ($CuSO_4$) resistive divider and an embedded Rogowski coil in the wall of the vacuum chamber, respectively. The axial end of the vacuum chamber was sealed with the use of 35.6 cm diameter O-ring and SS blank. Sampled power and frequency measurements were not made for this stage of experimentation.

4.1.1 Solid Cathode Prototypes

The SC-1, Fig. 4.2B, was a hollow-sheet copper design made to minimize the mechanical moment of the large structure attached to the 30 cm long cathode stalk. The design which is (36 cm X 8 cm X 13 cm) was made to maintain a 2 cm AK gap in both the cylindrical and planar regimes.

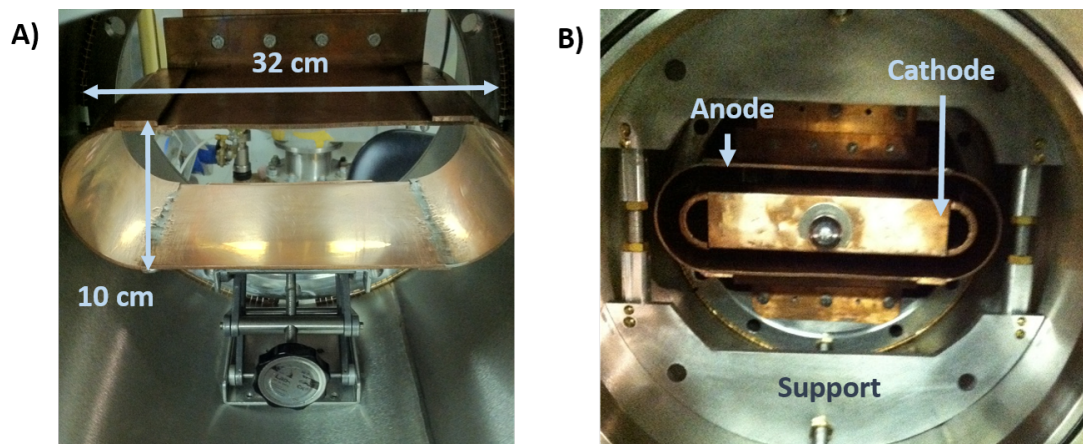


Figure 4.2. Photographs of: A) the smoothbore RPM anode, and B) the full smoothbore assembly with the SC-1 cathode.

The LC-1 is a more conservative cathode design intended to reduce the net current emission during the operation of the RPM. The LC-1, shown attached to the cathode stalk in Fig. 4.3A, is constructed of 1.28 cm thick 6061-Aluminum and is 25 cm X

15 cm featuring 0.64 cm radius fillets around each boundary. The LC-1 presented an AK gap of 4.4 cm when installed with the smoothbore anode, Fig. 4.3B.

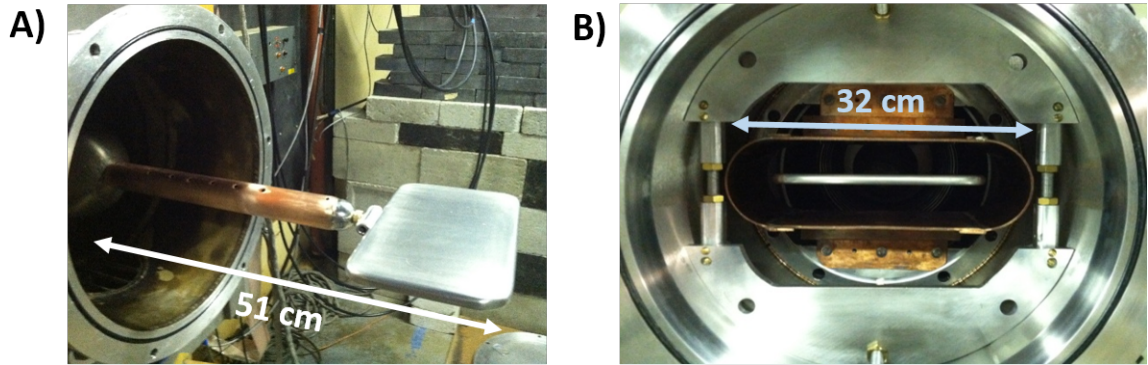


Figure 4.3. Photographs of: A) the LC-1 cathode and cathode stalk, and B) the full smoothbore assembly with the LC-1 cathode.

4.2 Magnetron Anodes: RPM-12a

The RPM-12a is a 12-cavity device composed of two sets of six Cartesian cavities made from 6061-Al. Each vane and cavity are 1.92 cm by 6.3 cm and is 11 cm in axial length corresponding to a resonant frequency of 1.01 GHz in pi-mode and an RF phase velocity of 0.26 c. The AK gap using the LC-1, depicted in Fig. 4.4, is 3.8 cm in both the planar and cylindrical regimes.

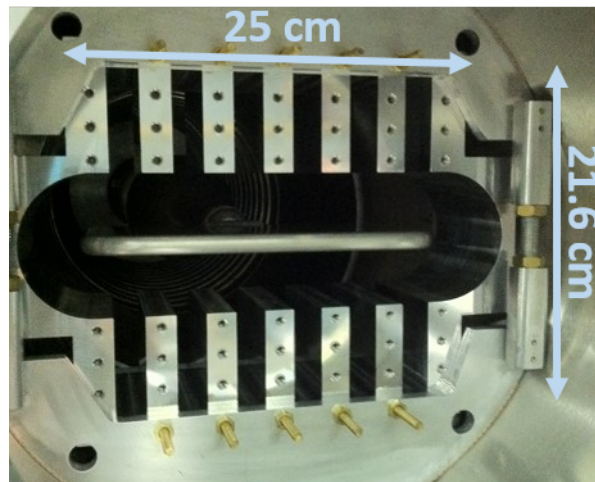


Figure 4.4. Photographs of the full RPM-12a assembly with the LC-1 cathode.

Similar to the smoothbore anode, the RPM-12a experimental setup in Fig. 4.5(A-B) made voltage and current measurements using the same $CuSO_4$ resistive divider and Rogowski coil. Pulsed, concentric electromagnets are spaced approximately 21.6 cm apart to form an approximate Helmholtz pair and provide a nearly uniform axial magnetic field, adjustable between 0.1 and 0.3 T [77]. In the Helmholtz magnetic field configuration, B varies in magnitude with respect to radial distance from the central axis of the electromagnets. The resultant decrease in magnetic field from the center of the device to the exterior recirculation region was found to be approximately 10 % of the peak on-axis field.

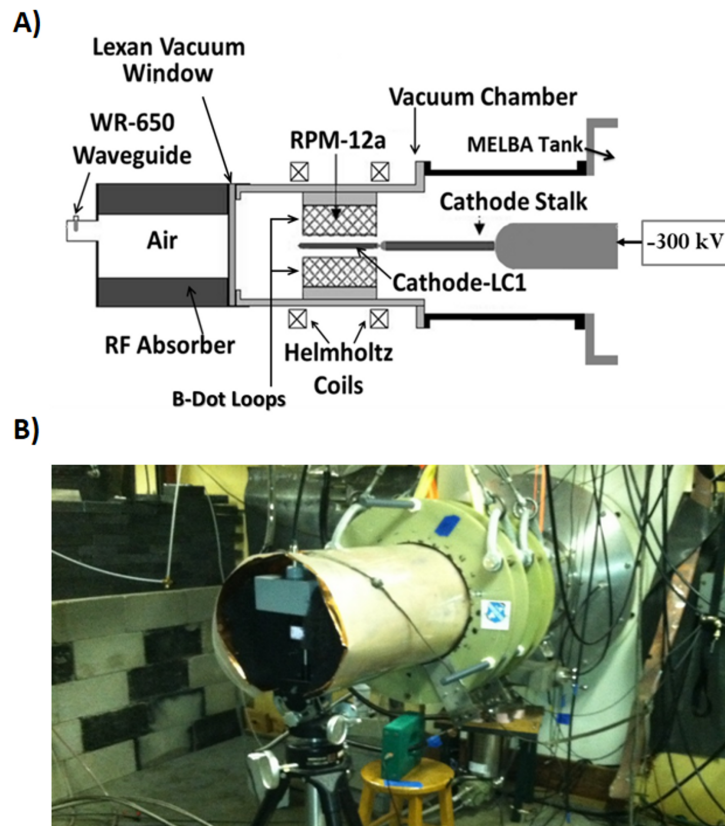


Figure 4.5. A) Experimental equipment diagram of the RPM-12a with diffraction coupling, and B) Exterior photograph of the experimental assembly in (A).

The # 304 stainless steel vacuum chamber, 63.5 cm in length, has an inner diameter of 39.4 cm and with cryopumping is capable of sustaining vacuum between 6×10^{-7} and 4×10^{-6} Torr. The chamber terminates into a transparent, 2.54 cm thick, Lexan window, which seals to the same o-ring interface as the SS blank on the outermost flange. The inner surface of the copper load chamber is coated with an 8 cm-thick annulus of microwave absorber (Ecosorb) in order to dissipate microwave power outside of the vacuum system. The experimental anode prototype RPM-12a is centered in the vacuum chamber with the Cathode-LC1 extending into the mid-plane between the planar slow wave structures. Dielectric fibers were attached to the cathode in 10 cm strips approximately 1.9 cm wide to match the width of the anode vanes. A total of six strips, with three placed underneath every-other vane on both sides of the cathode, were used to enhance π -mode oscillations via cathode emission priming shown in Fig. 4.6 [78].

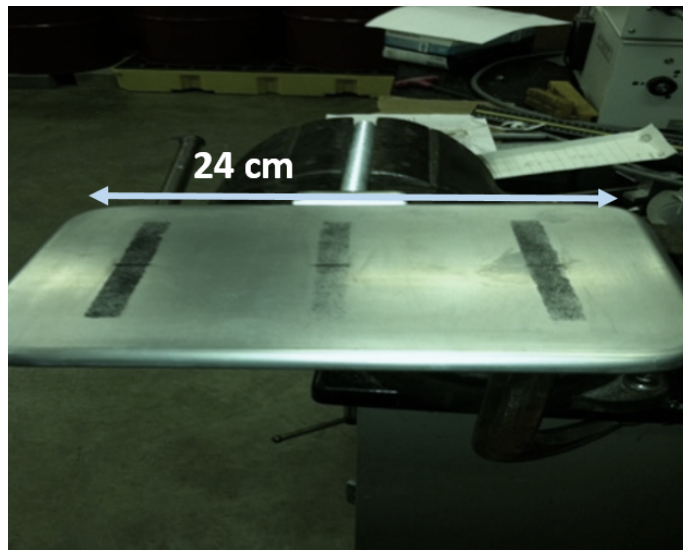


Figure 4.6. Photograph of the LC-1 with dielectric fiber emission priming sites.

The open-cavity configuration of the RPM allows for generated microwave pulses to radiate freely (albeit inefficiently) into the vacuum chamber from both sides of

the anode via diffraction coupling [79, 80] . Microwave pulses traverse out of the vacuum chamber, through the Lexan window, into the load chamber before coupling to a WR650 waveguide with type-N receiving antenna into RG-213U coaxial cable. The signal is processed in the Faraday cage using a series of type-N attenuators between 40 to 65 dB down before being split and input to separate frequency and power diagnostics. Frequency is observed using a heterodyne detector, which mixes the attenuated microwave pulse with a 1.2 GHz, 10 dBm CW signal from an Agilent E4422B signal generator. The attenuated microwave signal is rectified by a calibrated Agilent 8472B diode detector, from which sampled RPM power is established. Axial electron endloss was measured by a Pearson coil (Model 410) connected to a (36.6 cm X 10.2 cm) current collector mounted on the inside of the Lexan window. B-dot loops were also installed in close proximity to the open face cavities in order to measure the fringe RF field being generated by the magnetron. The loops were oriented to observe the H_x field, which is generated by the dE_y/dz (the decay of the electric field in the cavity as one moves axially away from the device). Each loop had approximately 2 mm^2 area and was placed 3.75 cm away from the RPM-12a anode on the central cavity of either oscillator as depicted in Fig 4.7.

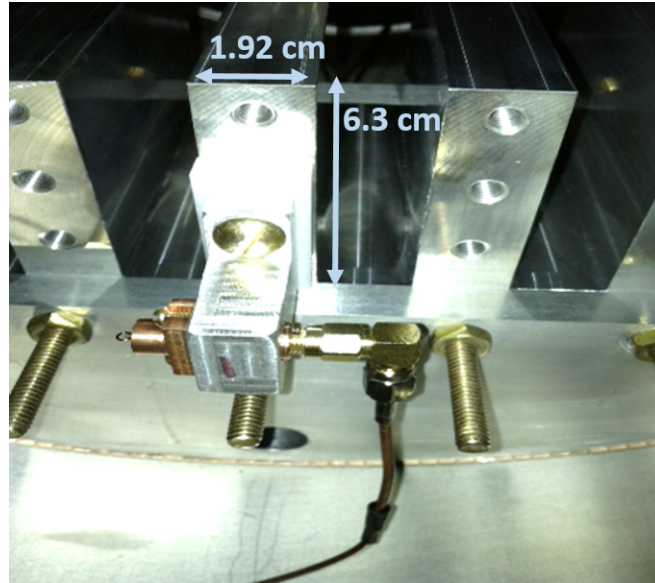


Figure 4.7. Photograph of experimental B-dot loop on the central vane of the bottom oscillator of the RPM-12a.

The signal from either B-dot loop was processed for frequency and phase information by applying 25 to 35 dB of attenuation before recording the data on a Tectronix, TDS7404, 4 GHz oscilloscope. The scope, which is readily capable of resolving the two raw 1 GHz signals, allows for a measurement of relative phase between either oscillators, which is used to diagnose phase locking within the RPM.

4.2.1 Cathodes: MCC-1

The first mode control cathode prototype, in Fig 2.8A, was composed of 5 hollow 6061 Aluminum rods, each of which had an outer diameter of 2.22 cm. The rods were structurally bound by pressure-fitting the ends of the array into 5 cm OD cylindrical endhats. The endhats, which extended a transverse length of 25 cm, featured domed ends (2.54 cm radii) to inhibit field enhancement and were partially hollowed on the interior side to reduce the weight of the assembly. Glyptal coating was added to the regions for which electron emission from the cathode were not desirable, most

notably the endhats and some portion of the axial ends of the cylindrical array of hollow aluminum rods [81]. The Glyptal-coated MCC-1 is shown installed in the RPM-12a experimental assembly in Fig. 4.8B.

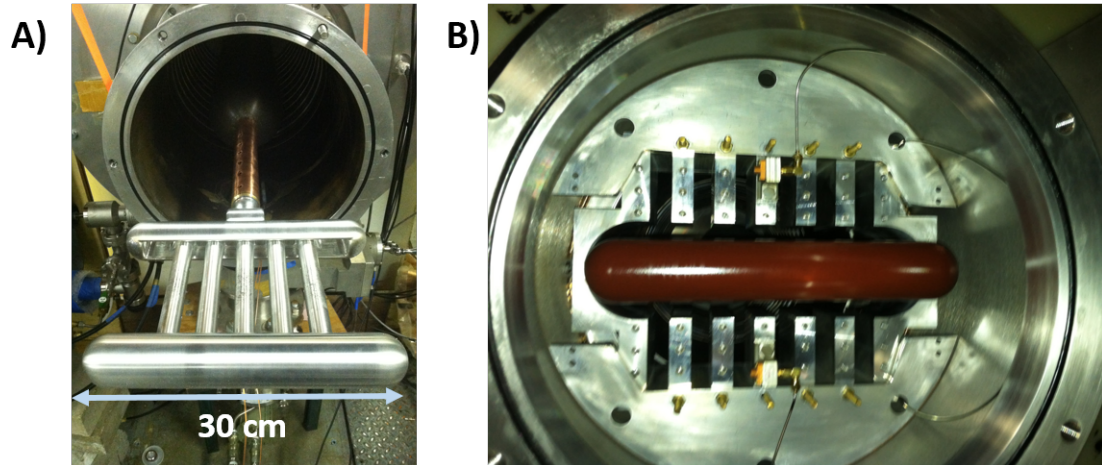


Figure 4.8. Photographs of: A) the MCC-1 cathode and cathode stalk, and B) the full RPM-12a assembly with the MCC-1Lg (Glyptal coated).

The MCC-1 was originally built with a 15 cm axial separation between the cylindrical endhats. This limited axial length induced undesirable electron emission from the cylindrical endhat to the cylindrical regions of the RPM-12a anode. Pulses that generated high currents in this manner caused considerable damage to the anode, which is shown in Fig. 4.9.

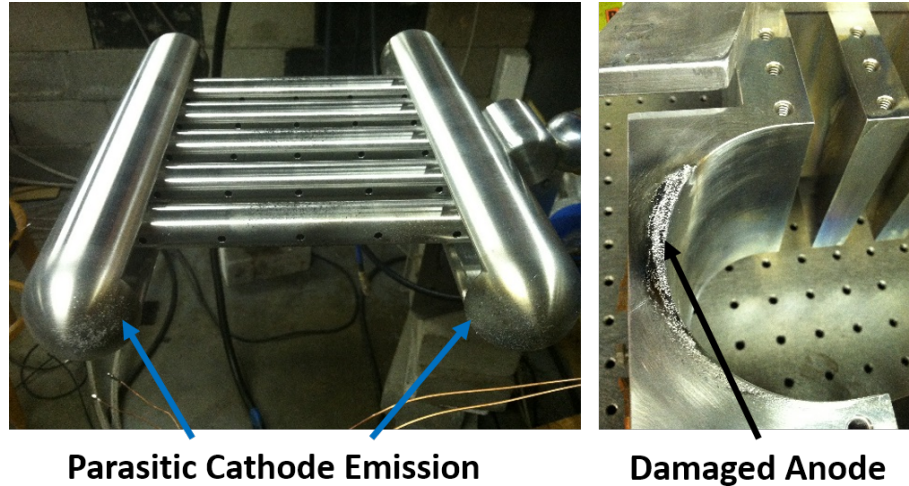


Figure 4.9. Experimental photographs of damage caused by arcing to the cathode (left) and anode (right).

The potential of the MCCs endhats to cause damage to the anode was alleviated by extending the length of the aluminum rods from 15 cm to 20.3 cm. Due to the operational difference caused by the additional separation of the endhats, the lengthened cathode is denoted as the MCC-1L. The Glyptal coated MCC-1L is referred to as the MCC-1Lg to distinguish the low current variant.

4.2.2 Cathodes: MCC-2

The MCC-2, in Fig 4.10(A-B), was an adaptation of the MCC-1 designed to reduce the AK gap of the RPM-12a which had a fixed separation between slow wave structures of 9 cm. The larger cathode design required a slightly more complicated design to achieve acceptable weight, which is detailed in (Appendix-A). The cathode in general houses five rectangular aluminum structures 1.91 cm X 3.83 cm, creating an effective AK gap of 2.6 cm. The cathode spanned 20 cm in axial length and was terminated by rectangular plates (19.5 cm X 5.3 cm X 1.2 cm) which were filleted about every edge. A Glyptal coating was also applied to the surface of the MCC-2 with the exception of an emission region in the central 5 cm.

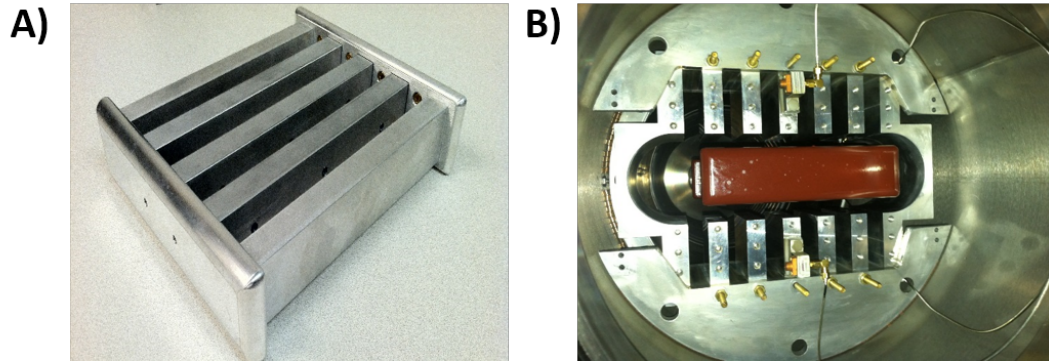


Figure 4.10. Photographs of: A) the MCC-2 cathode, and B) the RPM-12a assembly with the MCC-2 cathode.

4.3 Extraction: Coaxial Proof of Principle

The proof of principle extractor utilizes the RPM-12a and MCC-2 assembly shown in Fig. 4.9B. The inner conductors of the coaxial transmission (CTL) lines are composed of cylindrical 1.5 cm OD aluminum bar stock are mounted to the central vane of either anode by 1/4 in-20 threaded rod, 3 cm above the tip of the vane. Each inner conductor extends 28 cm in axial length and terminates via a banana-jack connection with the DFA-650b. The outer conductor of the CTL, mounts directly to the chamber end plate and is made from 5 cm ID copper tube for assembly purposes. Power coupled to the CTL is converted from the TEM mode to the TE_{10} mode in the WR-650 via the inline DFA-650b coaxial-to-waveguide coupler. The TE_{10} forward propagating power is sampled using -60 dB directional loop couplers used in previous L-band magnetic priming experiments [18, 82]. The HPM pulse then propagates into a matched load (Ecosorb) with a return loss -10 dB over the operational bandwidth of 0.94 GHz to 1.01 GHz. An experimental equipment diagram and photo are shown in Fig 4.11A and Fig. 4.11B respectfully. The sampled signal from the directional-loop couplers is processed in the same manner as the previous experiment, featuring additional in-line attenuation before being fed into the calibrated Agilent 8472B

diode detector. Voltage and current measurements are made in the same fashion as the previous experimental iterations.

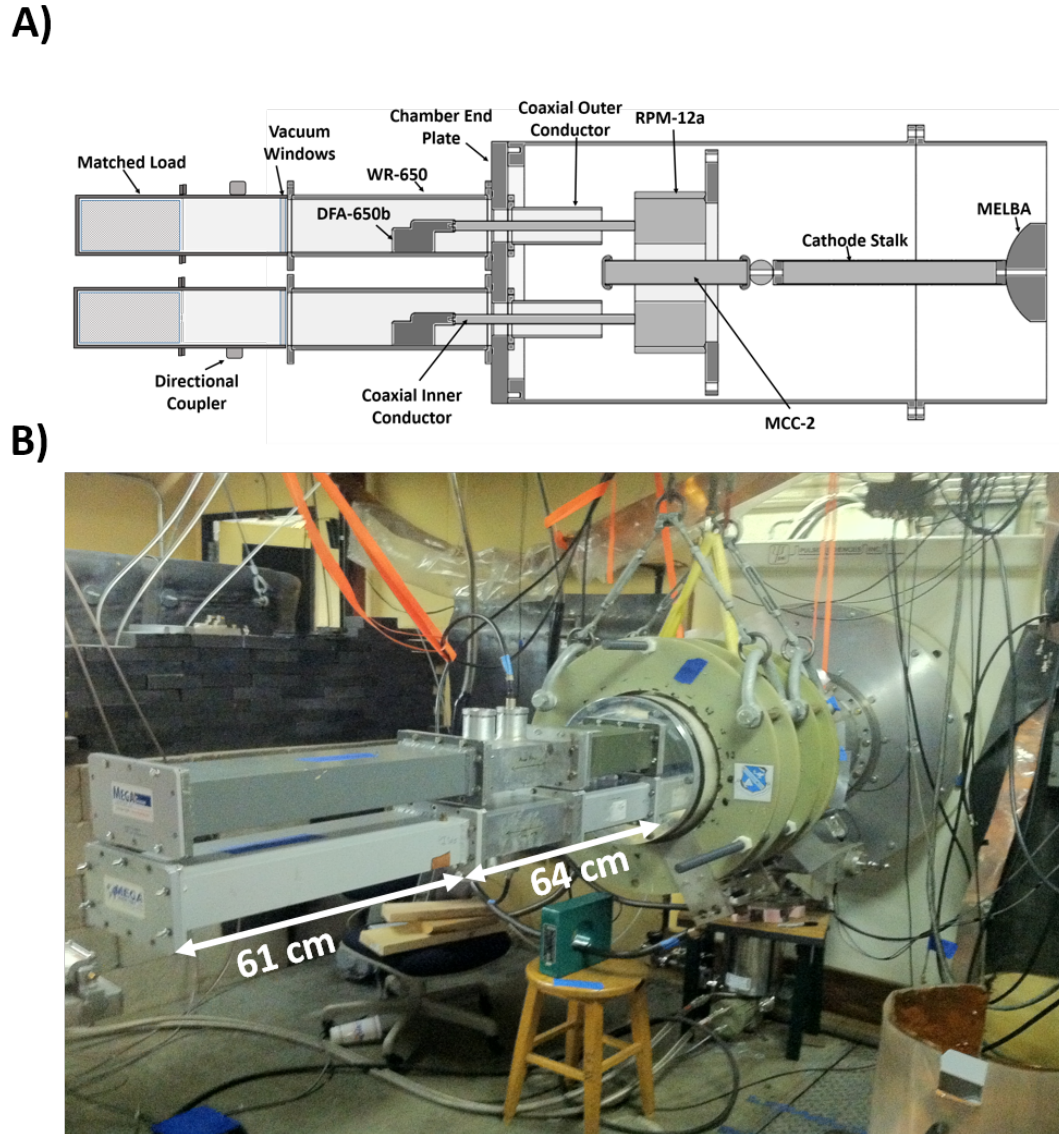


Figure 4.11. A) Experimental equipment diagram of the RPM-12a with coaxial extraction, and B) exterior photograph of the experimental assembly in (A).

4.4 Distributed Field Adapter

An experimental test setup was constructed using # 304 stainless steel in order to validate the transmission properties found in HFSS. The test setup shown in

Fig. 4.12 is composed of two DFA-340e couplers placed end to end such that power could be transmitted and received on either end of the device via WR340 to type-N waveguide antennas. The couplers are separated by 30 cm of coaxial transmission line, approximately $2\lambda_{fs}$ where $\lambda_{fs} = 15.8$ cm, in order to reduce the propensity of anomalous coupled modes from forming. Additional 33 cm lengths of aluminum waveguide were installed on each end of the setup to compensate for the large guided wavelengths, 38.8 cm, at 1.9 GHz in WR340.

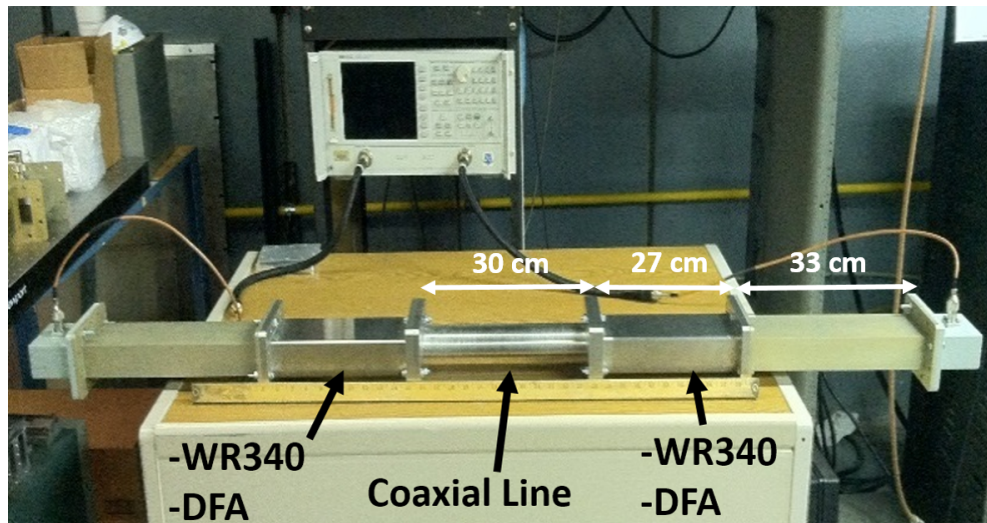


Figure 4.12. Photograph of the experimental test setup for the DFA-340e

The coupler, which is simulated to have a VSWR between 1.05 and 1.2, would have the same margin of reflection as the WR-340 to type-N waveguide antennas used to bring the signal out of the testbed assembly in Fig. 4.12. Due to the margin of error introduced by the experimental equipment, standard calibrations with the Agilent 350 mm cal kit could not be used, as it would only account for losses and reflections in the SMA-cables and not the antennas. Instead, a Transmission Line Through (TRL) calibration was performed on the 6772D Agilent Sweeping Network Analyzer (SNA)

[83]. The TRL process, which incorporates the Type-N to WR-340 antennas as well as the WR-340 aluminum straight sections of waveguide into the calibration of losses in the SNA, required the use of a perfect short, a straight section of transmission line with an electrical length of 90 degrees (where 20-160 degrees is acceptable), as well as a zero-delay assembly. Electric delay (θ), which is inversely related to the guided wavelength of WR-340, will go to zero as the operating frequency (f_0) approaches the TE₁₀ cutoff frequency (f_c) for a given spatial length (L),

$$(4.1) \quad \theta = L \frac{360f_0}{c} \sqrt{1 - \left(\frac{f_c}{f_0}\right)^2}.$$

A short was assembled using a # 6061 Aluminum WR-340 standard blank, while the through was formed from an additional length of 33 cm WR-340 waveguide to form a length of transmission line with a 53.5 degree delay.

CHAPTER V

Experimental Results

Data sets for the experimental RPM-12a are divided in four subsections corresponding to the cathode utilized during operation. These subsections include the solid cathode (LC-1), MCC-1, MCCL, and MCC-1Lg (schematics are shown in Appendix-A). Each experimental shot is evaluated on the basis of microwave startup-time, pulselength, and phase-locking duration. Experimental results for the DFA-340e (in-line coupler) and the Proof-of- Principle extraction system, equipped with the MCC-2, are also presented toward the end of the chapter.

5.1 Smoothbore Magnetron

Initial experiments were oriented towards controlling the net current emission and flattop voltage pulselength. The smoothbore anode was used in this preliminary study to ensure minimal field enhancement within the diode and to establish boundaries for pulse duration and gap closure, as well as magnetic insulation. The first solid cathode prototype (SC-1) was highly susceptible to parasitic emission and inevitably drooped the voltage to inoperable levels resulting in runaway pulses (non-crowbar shots) and arcing. This unstable operating environment was later corrected in the conservative solid cathode design (LC-1). The larger AK gap and polished Al-6060 surfaces resulted in very low current emission and controllable voltage wave-

forms without the use of parasitic emission inhibitors. Figure 5.1 is an example of a standard voltage and current waveform as a function of time for the smoothbore RPM and LC-1 cathode. The pulse reached approximately -300 kV at peak voltage and remained above -250 kV for 200 ns until command terminated at 900 ns. Currents during this voltage pulse reached 1.3 kA at the tail end of the pulse which demonstrated a significant reduction as compared to the 10-20 kA observed using the SC-1.

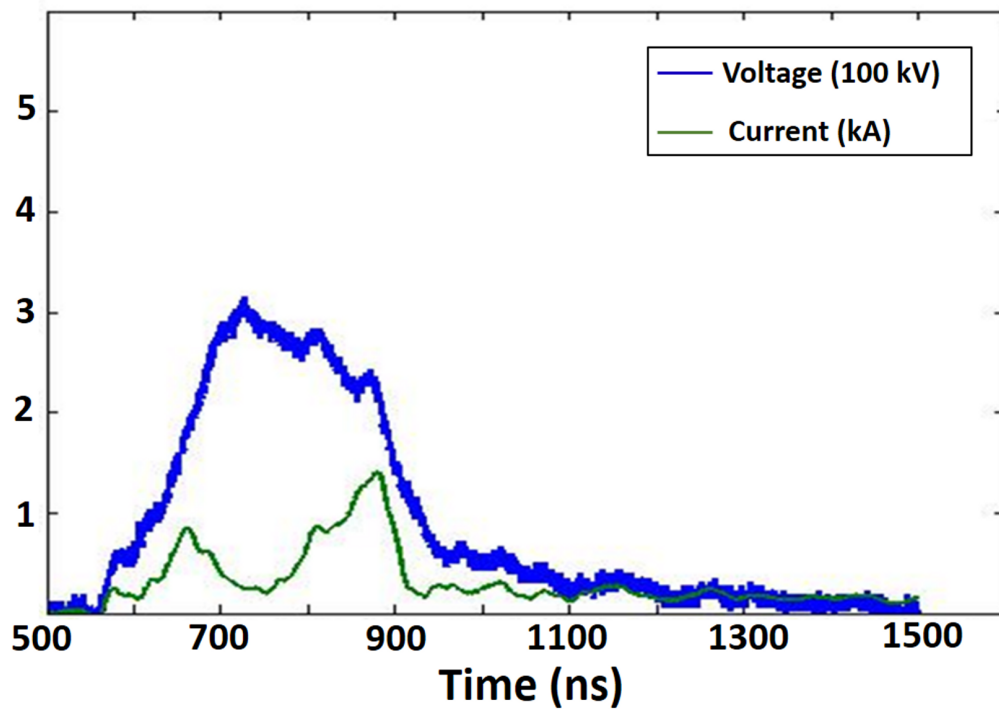


Figure 5.1. Experimental shot profile for the smooth bore RPM and LC-1 cathode with Voltage (blue) and Current (green).

The installation of the RPM-12a anode block in subsequent experiments led to increased current emission up to 3.2 kA as illustrated in Fig. 5.2A. Larger currents of 4-5 kA were achievable with the implementation of dielectric fibers in a π -primed pattern on either side of the LC-1, Fig. 5.2B.

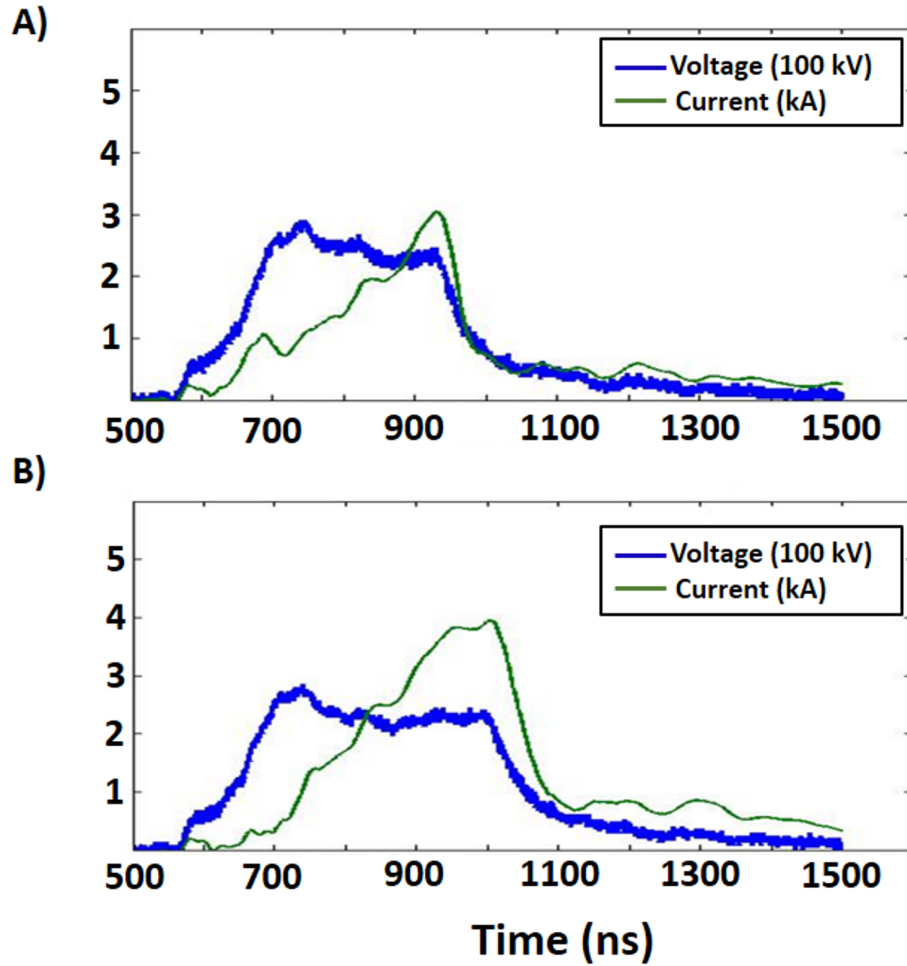


Figure 5.2. Experimental shot profile with Voltage (blue) and Current (green) for: A) the RPM-12a and LC-1 cathode, and B) The RPM-12a and LC-1 cathode with emission priming.

5.2 RPM-12a with LC-1 (Solid Cathode)

Simulated cold test results, shown previously, were verified using an Agilent sweeping network analyzer equipped with a simple dipole antenna; resultant $S(1,1)$ parameter scans are plotted on a decibel scale as a function of frequency in Fig. 5.3.

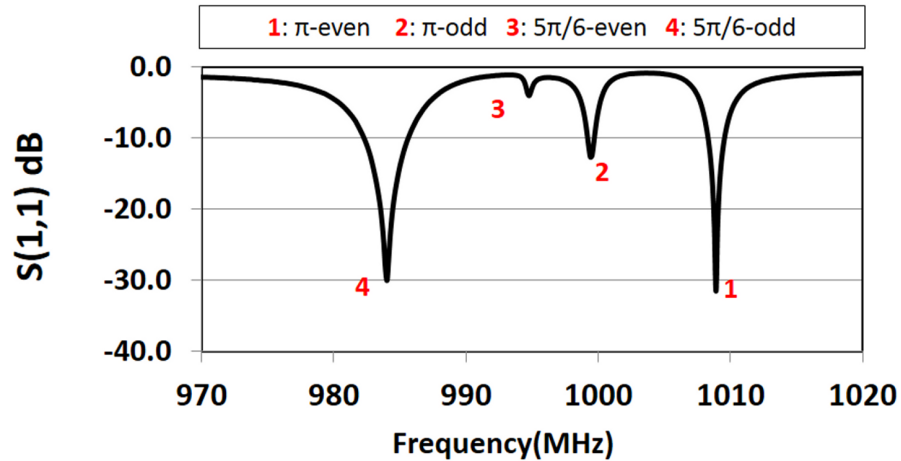


Figure 5.3. Experimental cold test data taken using the network analyzer equipped with a dipole antenna in close proximity to the RPM-12a cavities when installed in the vacuum chamber.

The primary area of interest is a 50 MHz window from 970 to 1020 MHz, in which the existence of 4 distinct modes were identified. Using the results from the full RPM-12a structure in HFSS we were able to roughly correlate these modes at 985 MHz, 995 MHz, 1002 MHz, and 1008 MHz to the even and odd $5\pi/6$, and π modes of the structure. The position of each resonance matches well with the simulated value with minor discrepancies of 3-8 MHz being attributed a perturbation due to the dipole antenna. Operational hot tests of the RPM-12a were also performed in order to correlate the operating beam-loaded frequency of the RPM-12a cold tube dispersion relation and other simulated hot tests. The LC-1 was operated between magnetic fields of 0.16 T and 0.22 T, corresponding to beam velocities that were substantial slower than analytically dictated in Fig. 5.4.

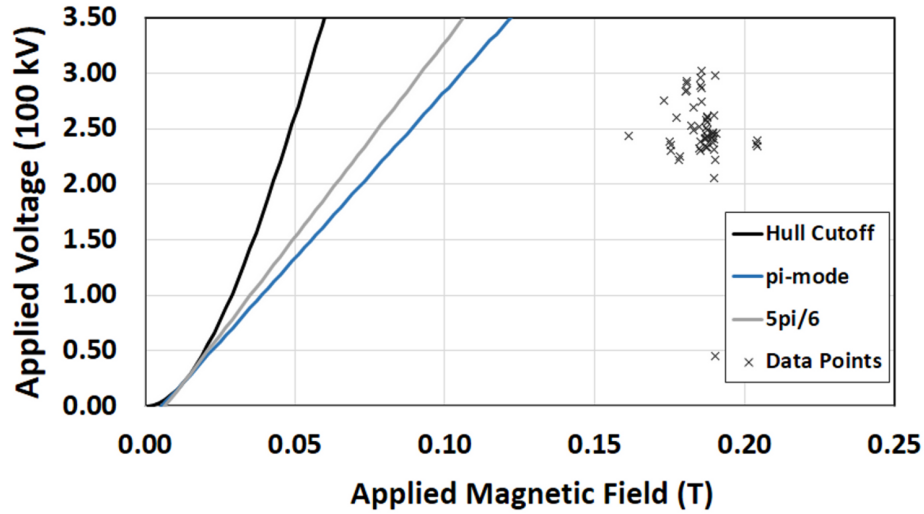


Figure 5.4. Buneman Hartree Curves for the RPM-12a π -mode (blue), $5\pi/6$ -mode (red), and Hull cutoff (black) overlaid with the operational positions of each solid cathode shot (black x).

Higher beam velocities, which would require a lower magnetic field or higher voltage, were not readily achievable in practice. Magnetic insulation was typically lost for applied magnetic fields below 0.15 T due in part to plasma gap closure [84]. Additionally, significant endloss emission in excess of 2 kA, from the LC-1 commonly induced a drop in the applied voltage during operation. This loss of cathode potential inhibited the ability to control pulse termination (crowbar) and inevitably led to full gap closure (shorting) between cathode and anode. Higher applied magnetic fields were still capable of generating microwave radiation as the electron hub expanded and eventually generated a drifting electron layer in synchronism with the RF wave. Excitation of the RPM-12a slow-wave structure in this manner required time to develop and delayed pulse waveforms as shown in Fig. 5.5 (A-D). The shot profile in Fig. 5.5A demonstrates even π -mode operation at 1.012 GHz using a -250 kV pulsed bias at 0.2 T axial magnetic field. Microwave radiation was not observed

until approximately 300 ns after the voltage rise, however, the HPM pulse itself was sustained for 250 ns with minimal interruption or mode competition.

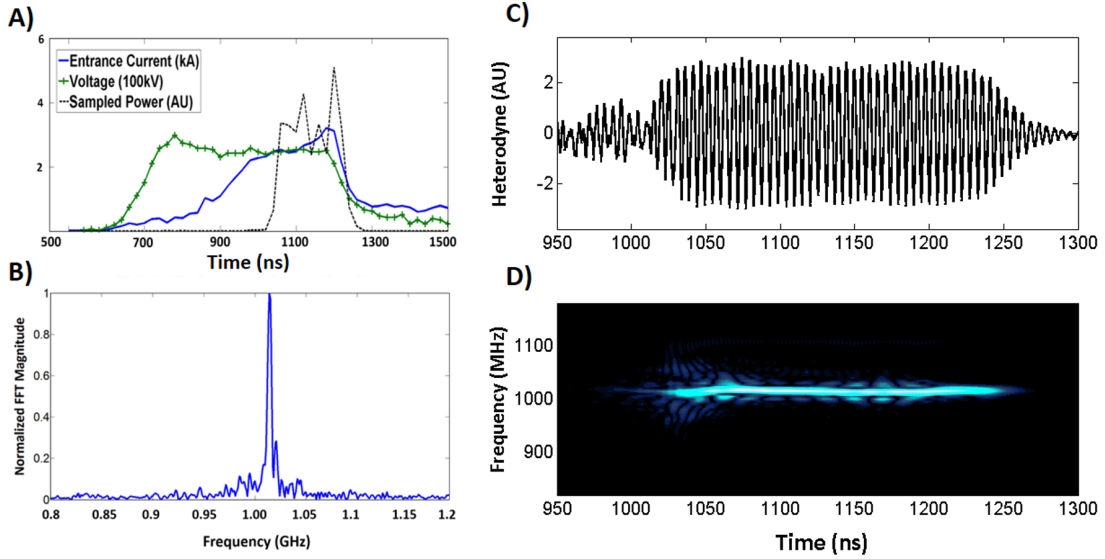


Figure 5.5. RPM-12a with LC-1 data: A) shot profile depicting voltage (green), current (blue), sampled power (black) as function of time, B) raw signal from heterodyne diagnostic, C) time-integrated Fourier transform, and D) time-frequency analysis (normalized white=1 and blue=0.5 and black=0).

Despite having many long uniform pulses as shown in Fig. 5.5 (A-D), the RPM-12a was still highly susceptible to intense mode competition. Figure 5.6 (A-D) demonstrates strong bi-modal operation at both 0.98 GHz and 1.015 GHz corresponding to the operating even π and $5\pi/6$ modes. Figure 5.6D illustrates that the pulse initiated at approximately 900 ns in π -mode before experiencing competition and eventual conversion to the $5\pi/6$ mode around 990 ns. Inevitably, the pulse demonstrated reduced levels of sampled power and a reduced pulselength of 120 ns, 40 % of the pulselength experienced by the single mode shot.

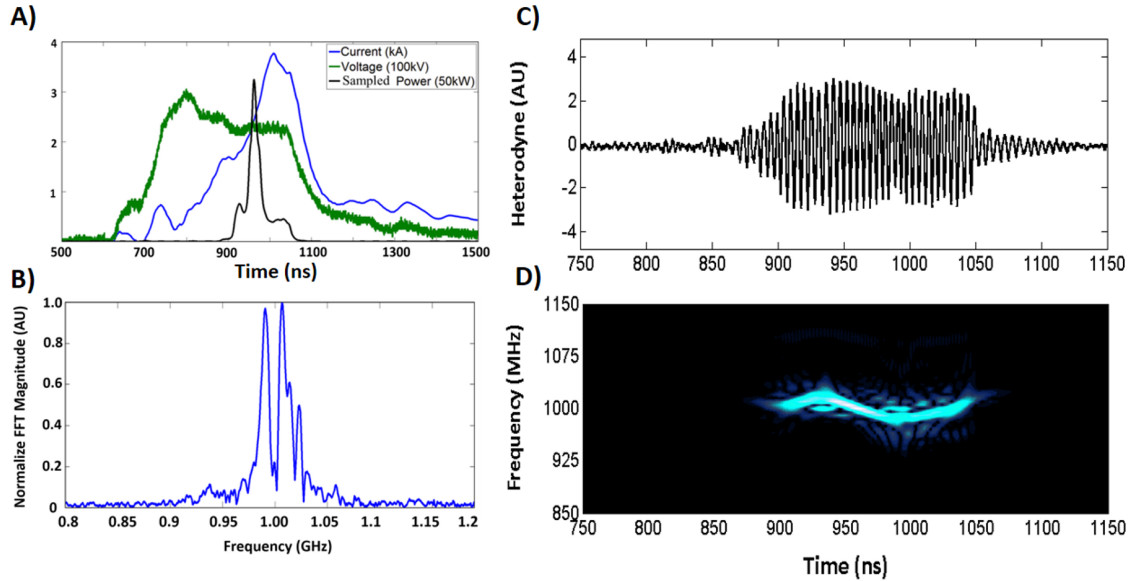


Figure 5.6. RPM-12a with LC-1 data: A) shot profile depicting voltage (green), current (blue), sampled power (black) as function of time, B) raw signal from heterodyne diagnostic, C) time-integrated Fourier transform, and D) time-frequency analysis (normalized white=1 and blue=0.5 and black=0).

A more in-depth analysis of these operating modes was performed by installing B-dot loops in close proximity to the central cavity on either oscillator as performed in magnetron experiments by Haworth, et al. [85]. The signal from each B-dot loop could then be directly compared to obtain a relative phase difference between each oscillator of the RPM-12a. Oscillators that failed to achieve locking from either mode competition or lack of cross-oscillator communication displayed a relative phase difference that drifted in time as shown in Fig. 5.7. The signal on the top oscillator, of the shot shown in Fig. 5.7, experienced a high degree of mode competition causing the signal to cycle on and off in the frequency range between 0.95 and 0.98 GHz.

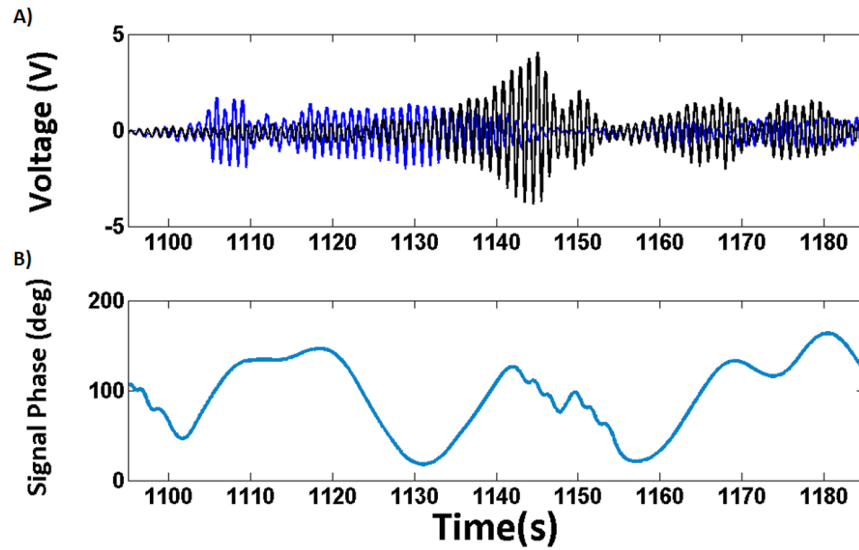


Figure 5.7. A) Raw data from B-dot signal on the top oscillator (blue) and the bottom oscillator (black), and B) relative phase difference between each B-dot as a function of time.

This mode competition is illustrated in Fig. 5.8, which shows that no unperturbed mode of operation existed for more than approximately 20 ns. The limited cross-oscillator communication provided by the LC-1 in conjunction with the highly irregular signal generated by the RPM made any type of locked oscillation impossible.

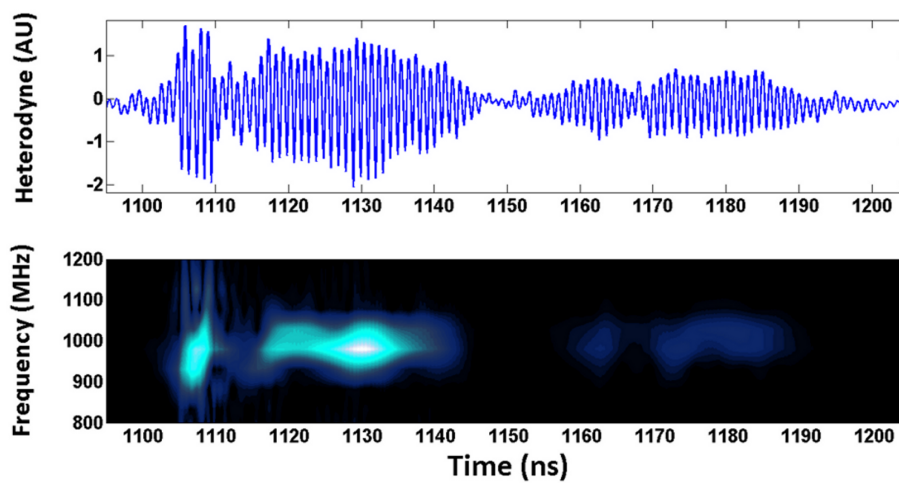


Figure 5.8. RPM-12a with LC-1: A) Raw data from the B-dot Signal on the top oscillator, and B) Time Frequency Analysis from the B-dot signal (normalized white=1 and blue=0.5 and black=0).

5.3 RPM-12a with Mode Control Cathode

The use of the MCC, which provides enhanced electromagnetic feed-through between oscillators, is designed to encourage phase-locking between the nearly identical strongly coupled oscillators of the RPM by reducing the time required to achieve a state of phase-locked operation [56]. Peer-to-Peer phase-locking has been demonstrated experimentally in both conventional 1 kW CW systems up to pulsed 1 GW sub μ s devices when the magnetron are strongly coupled [86, 87]. Experimental data detailed in this chapter demonstrate that long, uniform, pulses generated using the MCC cathode, such as the signal in Fig. 5.9, readily generated periods of phase locked operation. For the purposes of consistency, phase-locking is defined in our study as *a state of operation wherein the relative phase difference between each oscillator is static for durations greater than 20 ns with margins of error defined by ± 5 , 10, and 15 degrees.*

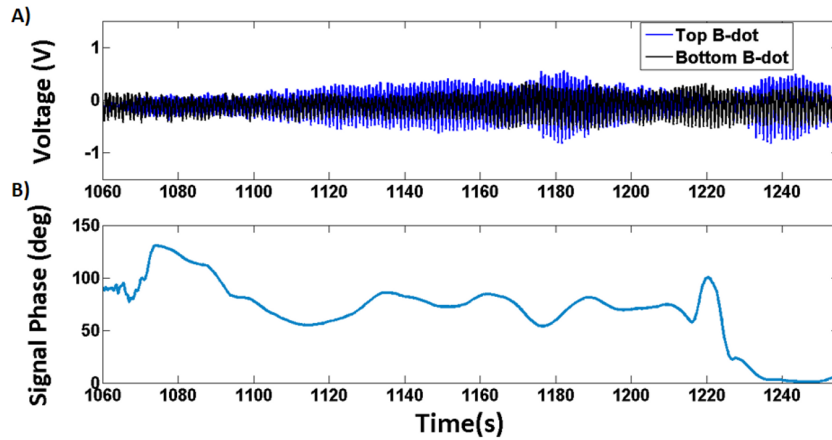


Figure 5.9. Experimental results from the RPM-12a with MCC-1 showing: A) Raw data from B-dot signal on the top oscillator (blue) and the bottom oscillator (black), and B) relative phase difference between each B-dot signal as a function of time.

Analysis of the shot depicted in Fig. 5.9 accentuates periods of phase locked operation from approximately 1140 ns to 1220 ns at a relative phase difference of 70 degrees and an additional period of phase locked operation from 1235 ns to 1260 ns with a phase differential of 6 degrees. Visualization of each locked-state of operation is more clearly illustrated in Fig. 5.10.

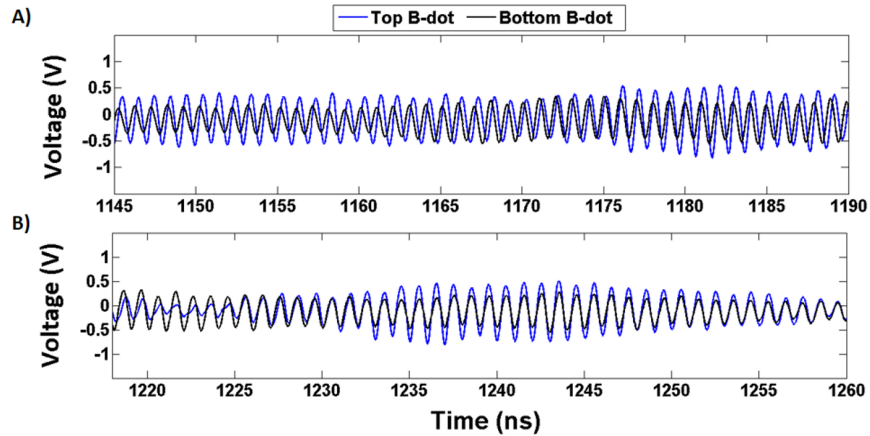


Figure 5.10. Zoomed in plots from Fig. 5.9A with the RPM-12a and MCC-1 depicting: A) Raw data from B-dot signal on the top oscillator (blue) and the bottom oscillator (black) during a state of phase-locked operation with a relative phase 70 degrees, and B) Raw data from B-dot signal on the top oscillator (blue) and the bottom oscillator (black) during a state of phase-locked operation with a relative phase 0 degrees.

A direct comparison can be made between the solid cathode (LC-1) and MCC by analyzing the duration of locking and average startup times for the microwave signal.

5.3.1 MCC-1 Cathode

Similar to the solid cathode, the first MCC prototype, MCC-1, was operated between 200 and 300 kV and 0.15 and 0.225 T as shown in Fig. 5.11.

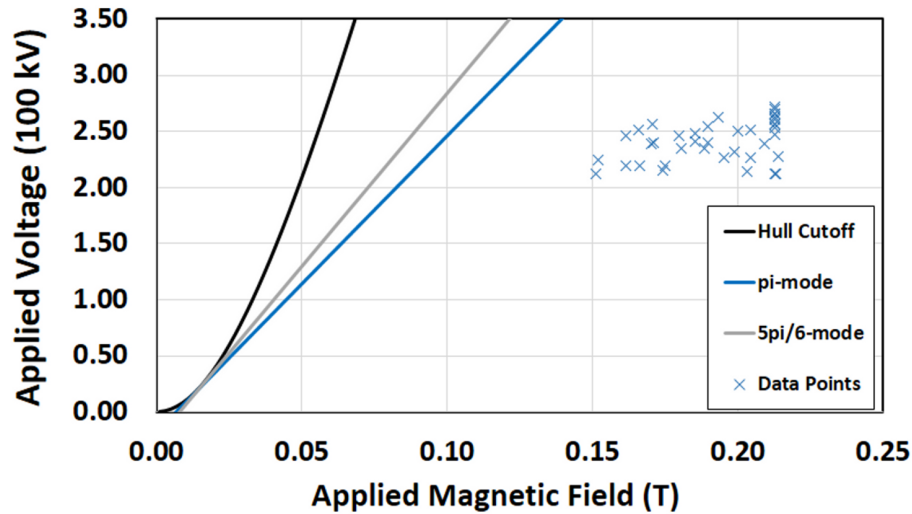


Figure 5.11. RPM-12a with MCC-1 Buneman Hartree Curves for: π -mode (blue), $5\pi/6$ -mode (grey), and Hull cutoff (black) overlaid with the operational parameters of each shot using the RPM-12a with MCC-1 (blue x).

The RPM faced the same dilemma with the MCC-1 as it did with the LC-1 solid cathode where in the large effective AK gap required magnetic fields that were well below achievable magnitudes. Operating at fields below 0.15 T resulted in the cathode endloss inhibitors arcing to the anode structure causing damage to both the cathode and anode. Preventative measures therefore required the MCC-1 be operated at high magnetic fields to excite the slow wave structure as the AK gap is reduced by gap closure.

Figure 5.12 demonstrates that the MCC-1 was capable of generating locked-states of operation that were consistently longer than the solid cathode for each margin of variation. The MCC-1 also demonstrated cases of less than 5 degree variation which was never observed using the solid (LC-1) cathode. The MCC-1 was observed to generate periods of locking within a 10 degree variation on 60 % of shots where both the top and bottom oscillator were generating microwaves for durations greater than

100 ns, whereas the LC-1 demonstrated 23 % based on the same criteria.

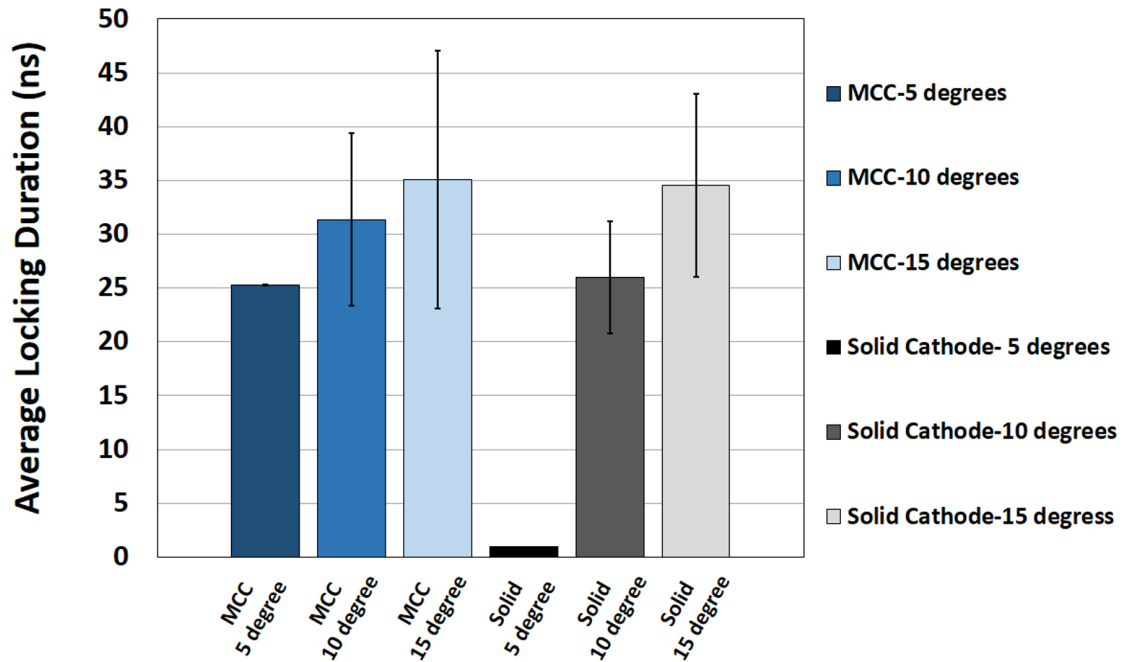


Figure 5.12. Comparison of average phase locked duration for relevant RPM-12a shots between the MCC-1 and the LC-1 for locking criteria of 5, 10, and 15 degrees.

The MCC-1 on average generated longer microwave pulselengths than the LC-1. Figure 5.13 depicts that the average microwave pulselength for the LC-1 was 124 ns while the MCC-1 achieved an average length of 260 ns. The endloss inhibitors, despite creating a strong susceptibility to anode-cathode arcing, evidently were able to confine the beam under proper operating conditions. The reduction in parasitic current not only increased the pulselength by 112 % but also showed faster startup times and higher sampled microwave diode powers.

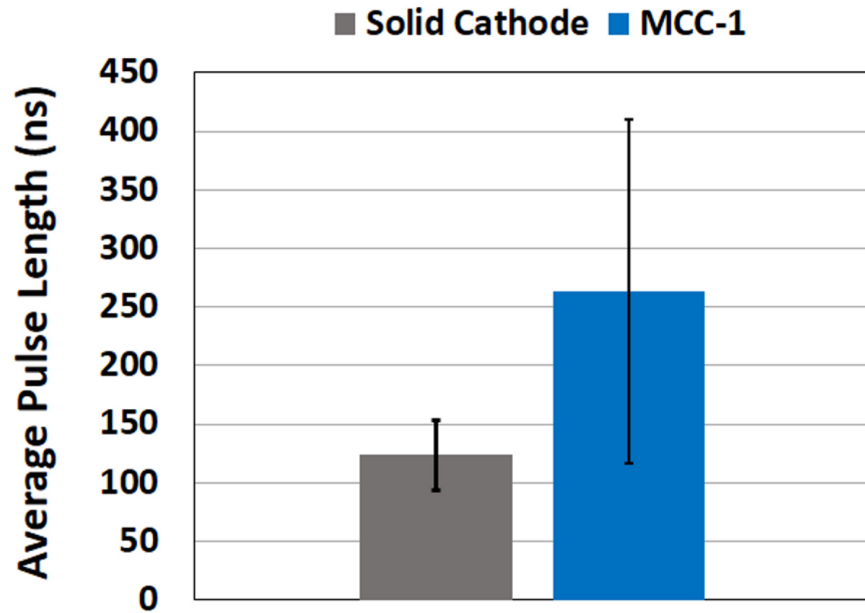


Figure 5.13. Average microwave pulselength for the RPM-12a with LC-1 and MCC-1 cathodes.

5.3.2 MCC-1L Cathode

The lengthened MCC-1L (20.3 cm), while successful in inhibiting arcing from the endloss inhibitors, was not able to reach controllable operation below 0.15 T. As a result, the range of externally applied fields used for operation of the RPM-12a with MCC-1L, plotted in Fig. 5.14, was very similar to that of the MCC-1, shown in Fig. 5.11.

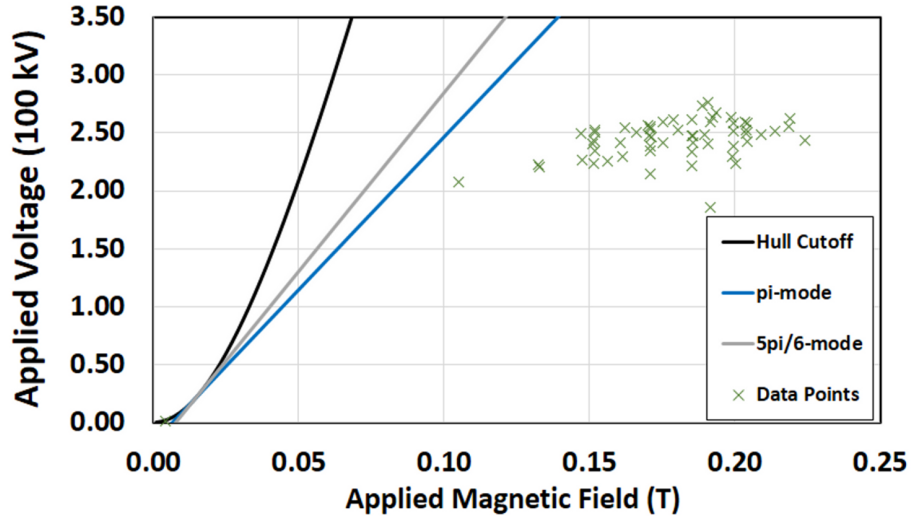


Figure 5.14. RPM-12a Buneman Hartree Curves for: pi-mode (blue), 5pi/6-mode (grey), and Hull cutoff (black) overlaid with the operational parameters of each shot using the RPM-12a with MCC-1L (green x).

The ability of the Mode Control Cathode to phase-lock oscillators appeared to be adversely affected by increased axial length of the MCC-1L. Fig. 5.15 summarizes the average locking duration for each phase criteria as compared to the LC-1. The MCC-1L produced instances of very stable locked operation of less than ± 5 degrees for an average of 26.5 ns, but failed to consistently achieve phase locking as readily as the MCC-1. Locked states of ± 10 degrees only occurred in 17 % and ± 15 degrees only occurred in 49 % of the shots whose microwave pulse durations exceeded 100 ns for both oscillators. Microwave pulselengths on average were decreased as compared to the MCC-1 to levels equivalent to those reached while using the LC-1 cathode.

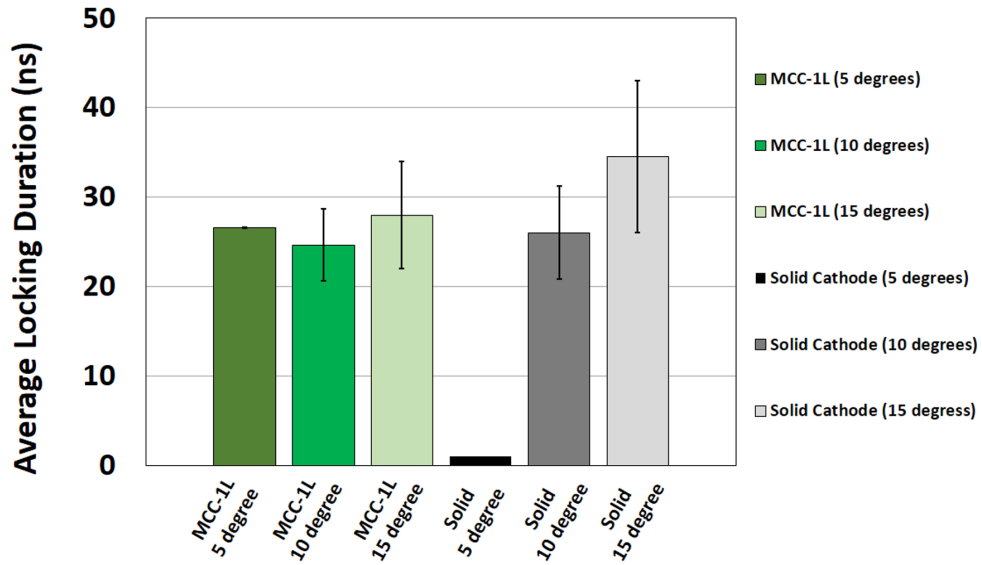


Figure 5.15. Comparison of average phase locked duration for relevant shots on the RPM-12a using the MCC-1L and the LC-1 for locking criteria of 5, 10, and 15 degrees.

Figure 5.16 shows that the MCC-1L attained only a minor advantage of 6 % average pulselength over that of the solid baseline cathode, LC-1, well within the error bars.

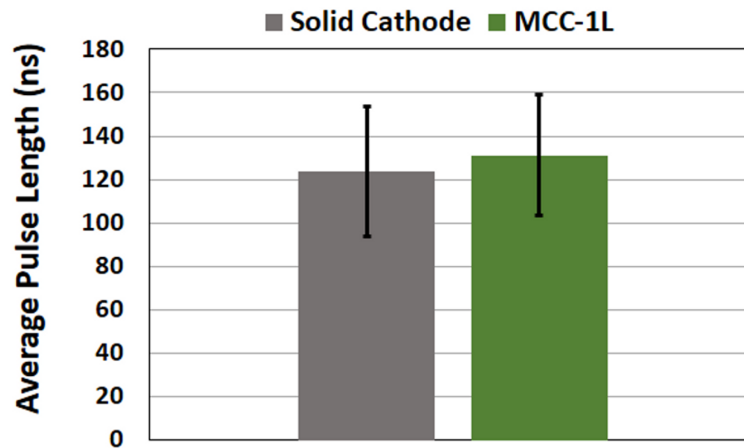


Figure 5.16. Average microwave pulselength for the RPM-12a using the LC-1 and MCC-1L cathodes.

5.3.3 MCC-1Lg Cathode

The application of Glyptal to the surface of the MCC-1L cathode (MCC-1Lg) significantly decreased the average current emission from 5.1 kA with the MCC-1L to 2.1 kA. The reduction in emitted current allowed for the application of lower magnetic fields to generate faster beam velocities without creating substantial drops in the pulsed voltage. The operating fields used for the MCC-1Lg are shown in Fig. 5.17 and show that applied magnetic fields between 0.15 and 0.17 were readily operable without significant drop in voltage or loss of control in pulse termination.

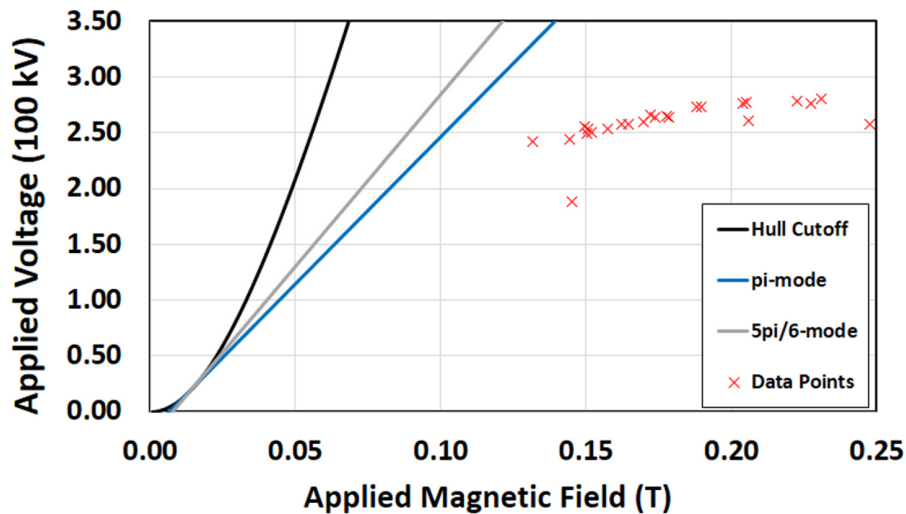


Figure 5.17. RPM-12a Buneman Hartree Curves for: pi-mode (blue), 5pi/6-mode (grey), and Hull cutoff (black) overlaid with the operational parameter of each shot of the RPM-12a with MCC-1Lg (red x).

The reduction of parasitic emitted current resulted in much faster startup of the microwave pulses within the RPM-12a. Figure 5.18 shows the average startup time for microwave oscillation in reference to the point in time at which the applied voltage reaches 175 kV. The microwave oscillations for the Glyptal coated MCC start up, on average, 400 ns faster than the solid cathode and nearly 200 ns faster than the

MCC-1. The long start up times for the solid cathode can be attributed primarily to the magnitude of endloss current out of the device which can adversely affect space charge bunches from readily forming. According the Fig. 5.18, the RPM-12a (with the MCC-1Lg installed) started up and, in some cases, terminated oscillation well before the voltage reached its peak value of 250-300 kV.

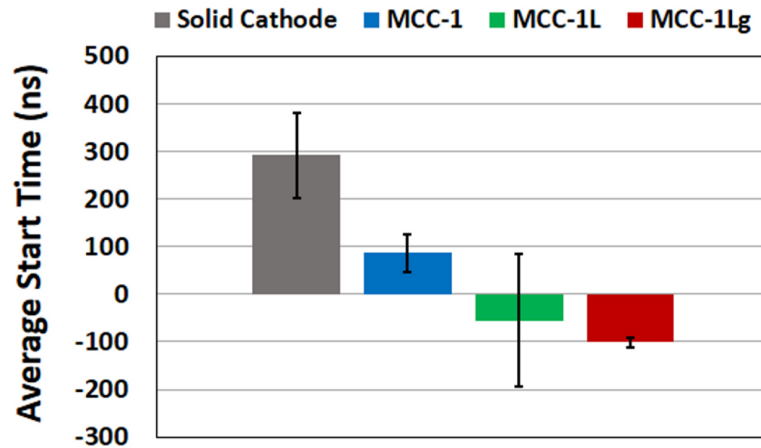


Figure 5.18. Relative startup time referenced to an applied voltage of 175 kV for the RPM-12a using: the solid cathode (grey), MCC-1 (blue), MCC-1L (green), and MCC-1Lg (red).

This rapid startup is likely attributed to both the lower operating magnetic fields, corresponding to a higher E/B drift velocity, and the highly controlled emission sites. The MCC-1Lg marginally improved the performance of the MCC-1L demonstrating increases of 15-30 % to the average locking duration of each classification and definitively improved operation as compared to the solid cathode in Fig. 5.19. The RPM-12a with MCC-1Lg cathode, despite generating lower currents, faster startup times and slightly longer durations of phase locking did not affect the mode separation of the highly competitive RPM-12a. As a direct result of this competition, many of the B-dot signals often generated pulses composed of two or more independent

frequencies.

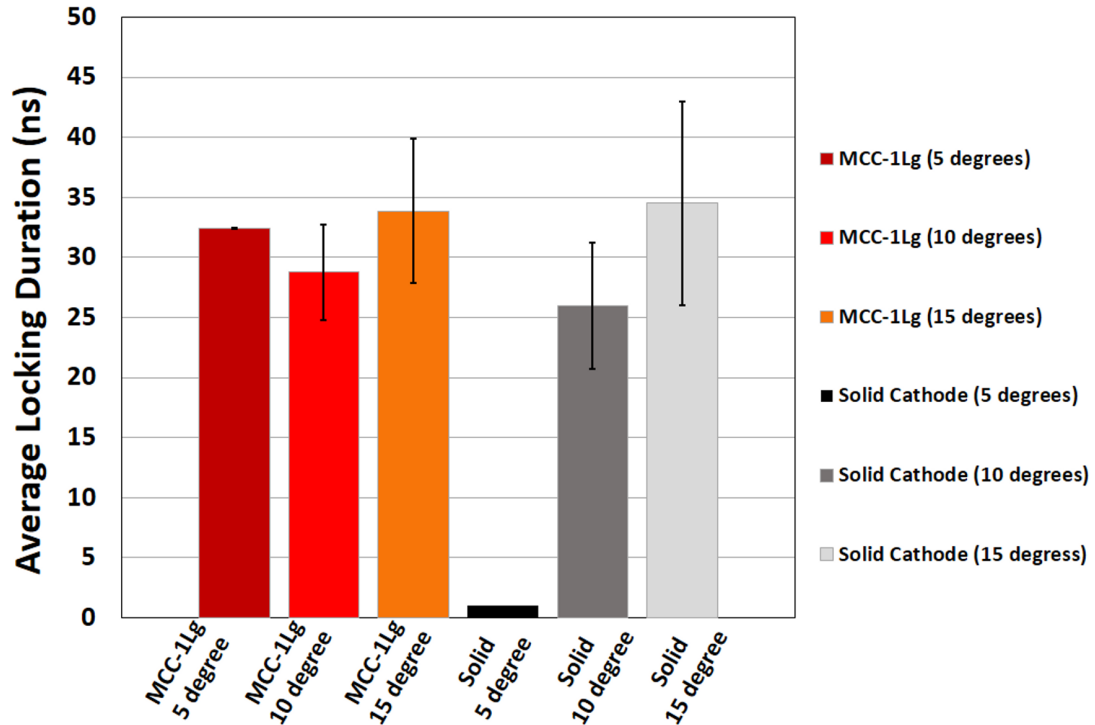


Figure 5.19. Comparison of average phase locked duration for relevant shots between the RPM-12a with the MCC-1L and the LC-1 for locking criteria of 5, 10, and 15 degrees.

This lack of consistency in the mode of operation, as has been demonstrated with previous cathodes, had a detrimental effect on the microwave pulselength and, subsequently, the potential for the cathode to phase-lock. The MCC-1Lg locked within ± 10 degrees on 25% percent of the pulses over 100 ns and on 62.5 % of those ± 15 degree range. Figure 5.20 shows that the addition of Glyptal had negligible effect on microwave pulselength as the duration over microwave oscillations for the MCC-1Lg is within 1 % of the MCC-1L.

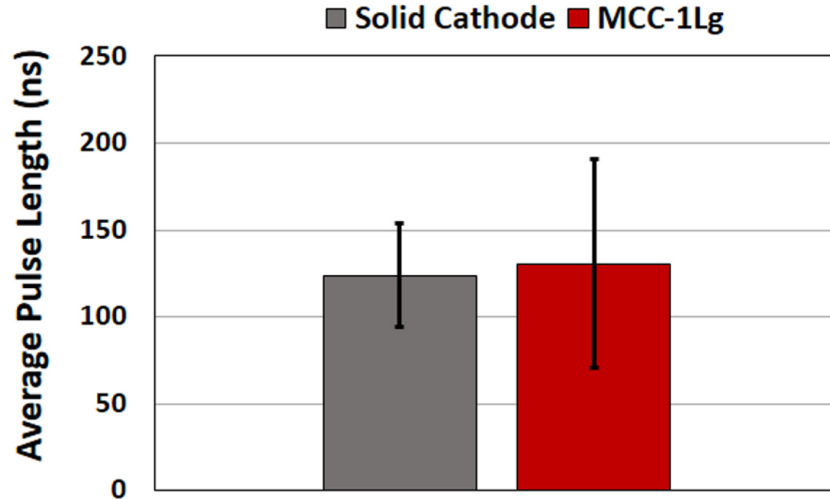


Figure 5.20. Average microwave pulse length for the RPM-12a using LC-1 and MCC-1L.

5.4 Overall Comparison of Cathodes on RPM-12a

The RPM-12a demonstrated a multitude of operating frequencies between 0.88 GHz and 1.13 GHz making the characterization of the operational dispersion relation difficult. Most shots, in order to initiate microwave oscillations, required the AK gap to partially close before the synchronous $\vec{E}X\vec{B}$ drift could be achieved. The lack of a known operational AK gap complicates arguments attempting to correlate the mode of operation to the applied voltage, as a given voltage generates a time changing electric field which is highly variable from shot to shot. Figure 5.21 illustrates the primary operating frequency of the RPM-12a as measured by the heterodyne diagnostic. According to this figure, 71 % percent of the measured shots using the solid LC-1 cathode operated at a frequency below 1 GHz, correlating to $5\pi/6$ and $2\pi/3$ modes. The MCC cathode measurements show only 56 % of shots operating below this 1 GHz threshold, suggesting a higher propensity to operate near or at π -mode.

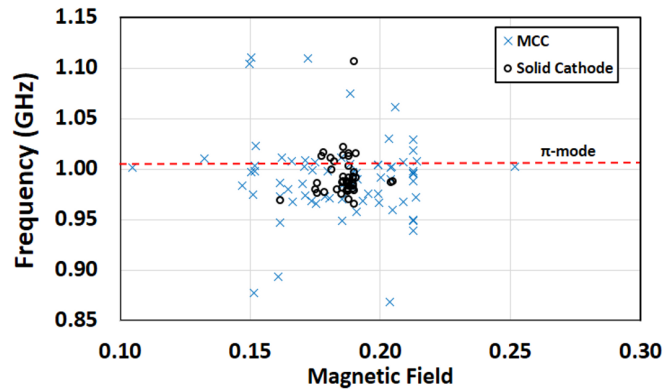


Figure 5.21. Operational frequency for each experimental shot on the RPM-12a as a function of applied magnetic field for the solid cathode (black) and MCC (blue).

Sampled power measurements, while not considered a means of viable power extraction, still provide some qualitative measure of how well the device is operating.

Figure 5.22 shows the sampled power magnitude in (MW) for each experimental shot, color coded for the use of each cathode.

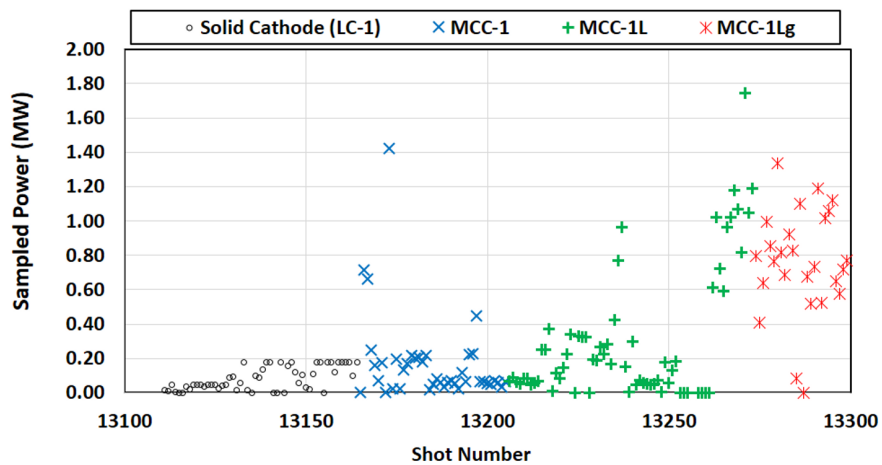


Figure 5.22. Sampled power measurements for the RPM-12a using a solid cathode (black), MCC-1 (blue), MCC-1L (green), MCC-1Lg (red), MCC-2 (purple).

The solid cathode averaged 80 kW reaching the WR-650 waveguide antenna, suggesting the generation of relatively weak microwave oscillations. Improvements in

sampled power measurements were observed in every stage of advancement for the MCC. The 0.18 MW sampled power observed with the MCC-1 was significantly improved upon by the MCC-1L and MCC-1Lg, which averaged 0.35 MW and 0.82 MW sampled powers respectfully. It should be noted that adjustments made to the MCC (MCC-1L and MCC-1Lg) allowed for operation at lower magnetic fields, closer to the theoretical synchronism condition.

5.5 Distributed Field Adapter: DFA-340e Testbed

The experimental DFA-340e testbed, which features two couplers placed in series, demonstrated good agreement with the same model simulated in HFSS over the frequency band of interest between 1.80 and 1.95 GHz. Figure 5.23 compares both the experimental and simulated two-coupler geometry to that of the single coupler simulated in Chapter 3. According to the (dotted) curve of Fig. 5.23, the inclusion of a second coupler promotes the transmission of RF power at higher frequencies as compared to the single, stand alone, coupler. This phenomenon is likely due to a trapped mode existing between the two couplers, which will not exist in the single coupler utilized in the RPM-340 CACE that utilizes only a single DFA-340e for each output transmission line.

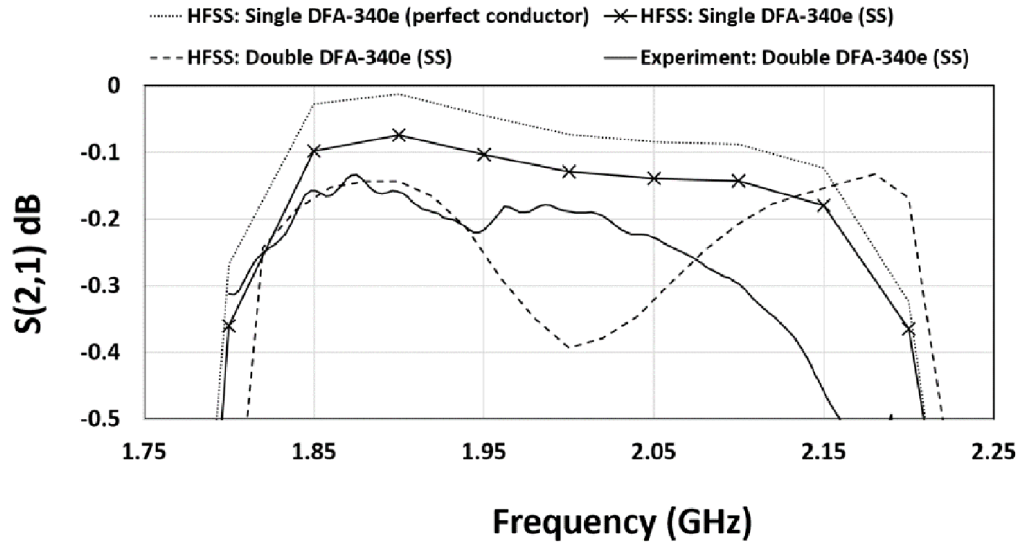


Figure 5.23. Transmission properties of the DFA-340e, comparing a simulated single DFA-340e made from perfect conductors (.), a simulated single coupler made from SS-304 (x), two simulated couplers adjoined together made from SS 304 (-), and two adjoined couplers made from SS304 in experiment (-).

The two-coupler geometry simulated in HFSS showed increased transmission at 2.1 to 2.2 GHz while the experiment demonstrated increased transmission from 1.95 to 2.05 GHz. The minor discrepancy between the simulated and experimental models (2-5 % in transmitted power) are likely due to the fabrication process, which introduces features such as welding joints between conductors, fillets around each edge, and minor manufacturing errors. The remaining deviation between the single and double DFA-340e is attributed to resistive losses due to the extra length of stainless steel.

5.6 RPM-12a Proof of Principle Coaxial Extractor

The proof of principle extractor, which featured Glytal coated MCC-2 cathode configuration was operated with applied fields ranging from 250-300 kV pulsed voltage and 0.17 to 0.22 T axial magnetic field. Lower magnetic fields necessary to achieve theoretical synchronism between the beam and RF wave, were (again) not

operable due to the increased current draw from the cathode. Despite the deviations from the theoretical guidelines, described in Chapters 2 and 3, the Proof of Principle (PoP) extractor produced higher powers than predicted with the particle-in-cell code, MAGIC. Peak extracted RF powers, combining the output of both the top and bottom waveguide, were observed in the range of 20 to 175 MW with total microwave pulse lengths ranging from 50-250 ns.

The operation RPM-12a with PoP extractor was categorized into two orientations of the anode and cathode, corresponding to the horizontal and vertical alignments shown in Fig. 5.24. The horizontal alignment, where the gravitational moment on the cathode caused the electrode to sag in the \hat{x} direction (affecting the AK-gap of the diode), was believed to be disadvantageous for phase-locking. The offset cathode in this configuration created an asymmetrical AK gap and resulted in dissimilar operating conditions between the two sides of the device. The vertical-configuration, where the misalignment is in the \hat{y} direction (affecting cathode/anode-vane alignment) was designed to eliminate this asymmetry.

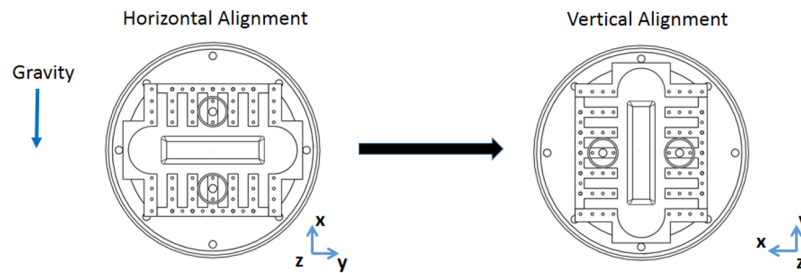


Figure 5.24. Experimental configurations of the RPM-12a with PoP extractor.

A shot profile of the RPM-12a with the horizontal-configuration of the PoP extractor is shown in Fig. 5.25. The image demonstrates that the generation of RF power was initiated just as the pulsed voltage reached its maximum at approximately 250

kV and produced a peak output power of 70 MW. The microwave-pulse, for both extractors, lasted for approximately 100 ns to 150 ns with an average power output of 50 MW for its duration. An analysis of the signals from both the top and bottom waveguide appeared to indicate the existence of strong competition between the two oscillators of the RPM-12a.

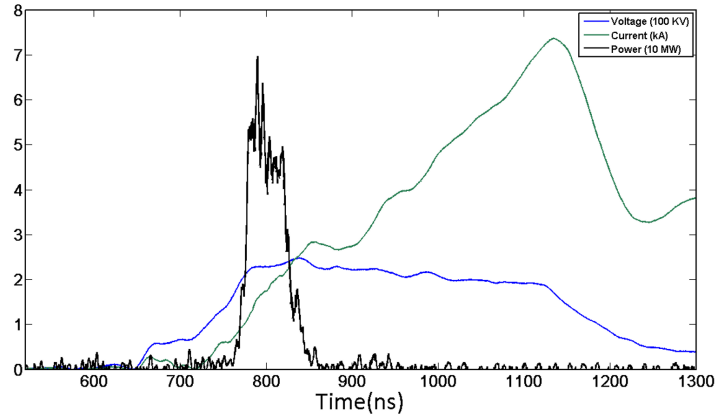


Figure 5.25. Shot profile for the horizontally-oriented RPM-12a with MCC-2 and PoP extractor depicting voltage (blue), current (green), and total microwave power (black) as a function of time.

Figure 5.26 illustrates that the bottom oscillator turns on first at 750 ns and rapidly decreases in signal strength at approximately 800 ns, at which point the top oscillator initiates generation of RF power for an additional 50 ns. Phase-locking the RPM-12a oscillators requires uniform operation of both slow wave structures simultaneously for durations in the range of 100 ns. The horizontal configuration, which was highly susceptible to competition between each oscillator, rarely achieved this state of operation and did not exhibit phase-locked operation.

An experimental series of 40 shots with the vertical configuration (identified by Fig. 5.24) readily demonstrated phase-locking. Periods of locking within a 10 degree variation were observed on 29 % of all shots over 100 ns, as compared to the 23 %

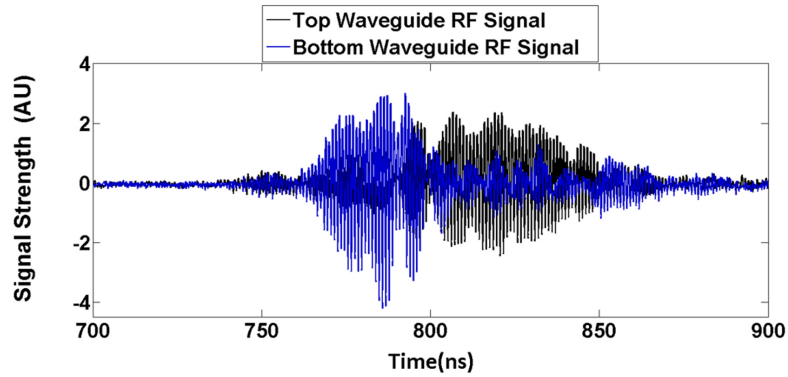


Figure 5.26. RF signal from the WR-650 directional loop couplers as measured from the top (black) and bottom (blue) waveguides in the PoP extractor on the horizontally-oriented RPM-12a.

observed with the solid cathode (LC-1). High power shots, in which extracted power exceeded 70 MW, exhibited an increased propensity for phase-locked operation (63 %) over lower power shots (10 %) using the same ± 10 degrees relative phase criteria. The average duration of phase-locking however, shown in Fig. 5.27, was lower than that of the solid cathode (LC-1) used in previous experiments.

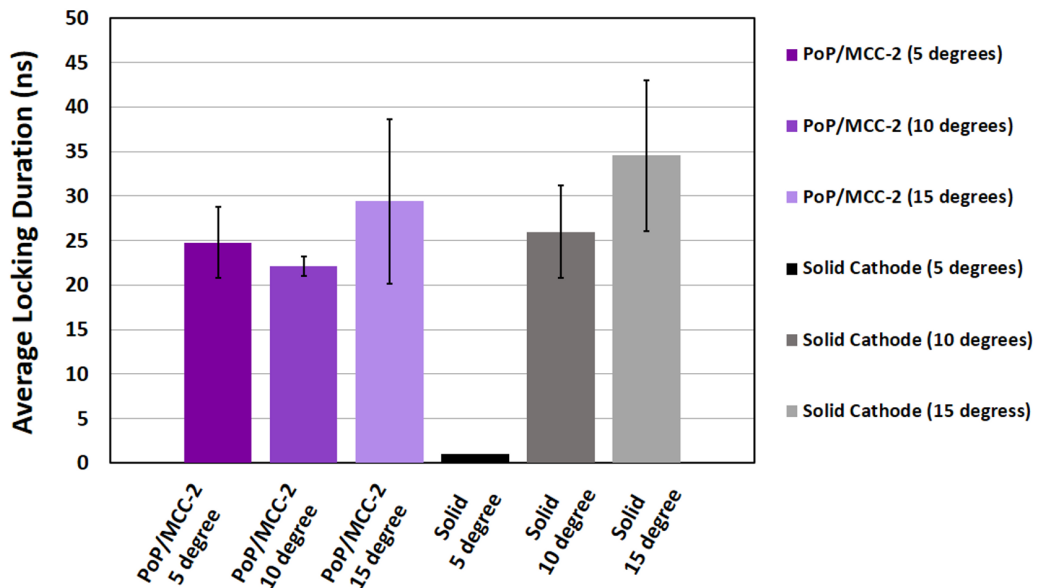


Figure 5.27. Comparison of average phase locked duration for relevant shots on the vertically oriented RPM-12a with PoP extractor using the MCC-2 and the RPM-12a with LC-1 for locking criteria of 5, 10, and 15 degrees.

The vertical configuration produced peak output powers of up to 151 MW, where a typical peak power of 60 MW was observed using the horizontal configuration. The increased output power, however, is attributed to conditioning of the MCC-2 cathode during operation and less so the alignment of the cathode.

Figure 5.28A, which relates output power chronologically with the shot number of the series (13333-13372), illustrates a trend of increased extracted power after shot 13354. The first twenty shots (13333-13353) yielded output powers in the range of 20-50 MW, which roughly matches the results gathered from the horizontal configuration. Operating the RPM-12a with a magnetic field below 0.17 T, shot 13353 according to Fig. 5.28B, resulted in a loss of magnetic insulation and full gap closure. Localized aluminum deposits on the surface of the MCC-2, due to the electrical arc, greatly enhanced the current emission from an average of 0.87 kA at peak power, before arcing, to an average of 1.69 kA at peak power in subsequent runs. The higher current emission from the MCC-2 resulted in increased extracted microwave power through the two output waveguides from a peak of approximately 80 MW to upwards of 151 MW, using the vertical configuration. The applied magnetic field was increased from shot 13354 to 13372 to compensate for the increased current emission from the cathode and to maintain electrical insulation in the diode.

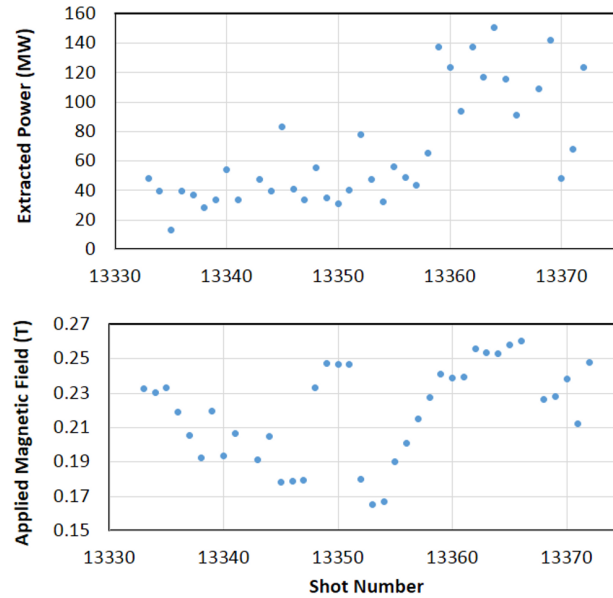


Figure 5.28. Experimental results for the vertical configuration of RPM-12a with PoP extractor and MCC-2 depicting: A) Extracted microwave power as a function of shot number, and B) applied magnetic field as a function of shot number.

The enhanced output power, post shot 13354, was observed on both oscillators (“left” and “right” side of the device from vertical configuration in Fig. 5.24), however, the left oscillator was observed to produce higher peak power on average. The shot profile in Fig. 5.29 shows that the output power on the left-oscillator reaches a peak value of 110 MW at 780 ns, while the right oscillator produced between 20 and 60 MW for the duration of the microwave pulse from 740 ns to 840 ns. This high power shot was observed to phase-lock in the even π -mode at 761 ns, corresponding to the initial rise in power of the left-oscillator (dashed red) shown in Fig. 5.29.

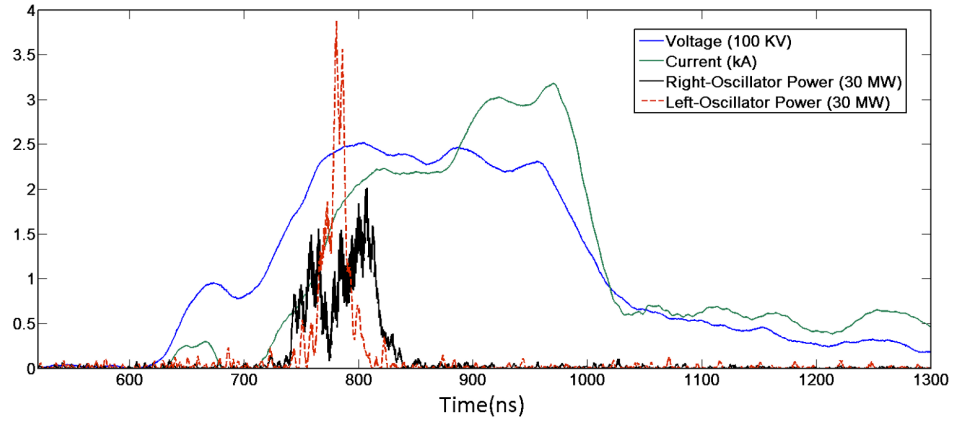


Figure 5.29. Shot profile for the RPM-12a with MCC-2 and PoP extractor depicting voltage (blue), current (green), output microwave power from the left-oscillator (dashed red), and output microwave power from the right-oscillator (black) as a function of time.

According to Fig. 5.30A, the RPM-12a with PoP extractor exhibited very high microwave power output (40-150 MW) at operating frequencies in the vicinity of the even π -mode, found in MAGIC PIC to be 0.993 GHz. Instantaneous peak efficiency for these even π -mode shots were between 10 and 42 %, given by Fig. 5.30B. A low power (40 MW), high peak efficiency (46%), shot was observed to operate at 0.979 GHz, corresponding to the odd π -mode in simulation. The efficiency measurements for the PoP experiment are based on the total emitted current from the MCC-2 and include both diode current and parasitic endloss current during operation. The existence of endloss current, which does not contribute to the generation of microwave power, would result in smaller currents within the diode itself and higher magnetron electronic efficiency. An isolated measurement of diode and endloss current was not feasible on the current PoP extractor system and remains a subject of future research.

High peak powers between 140 and 175 MW were also observed at 1.007 GHz, well above the even- π -mode. The asymmetrical external load imposed on the RPM-12a by the the coaxial extractors, discussed previously in Chapter 3, induces separation in

the resonant frequencies between otherwise degenerate modes in the device. Phase-shifted operating modes of the RPM-12a with PoP extractor, were identified at 1.01 GHz (even- $5\pi/6$), 1.025 GHz (even- π), and 1.045 GHz (odd- π) in HFSS.

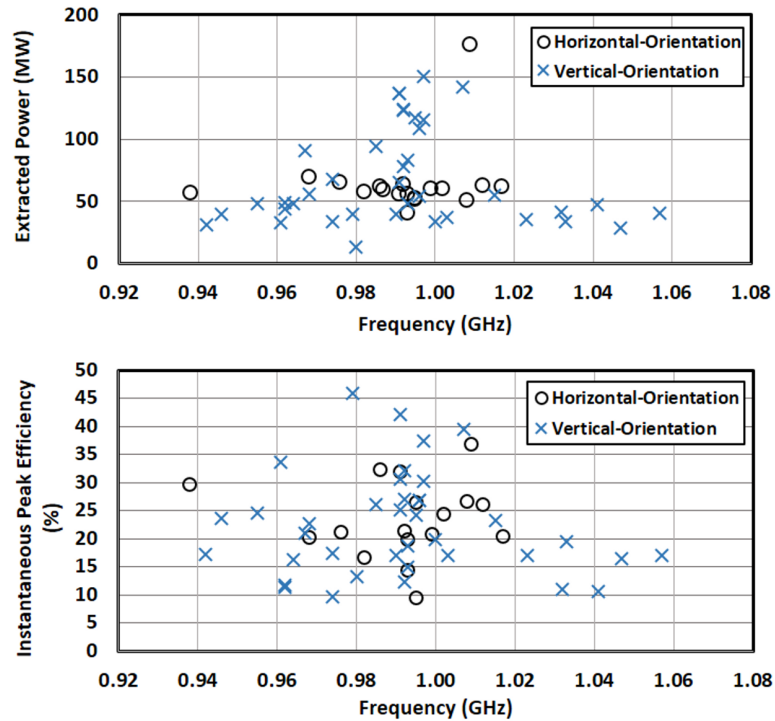


Figure 5.30. Experimental results for RPM-12a with PoP extractor and MCC-2 depicting: A) Extracted microwave power as a function of operating frequency, and B) instantaneous peak efficiency as a function of operating frequency for both the vertical (blue-X) and horizontal (black-O) configurations.

The resultant frequency spectrum is generated by the RPM over a wide range of applied magnetic fields, as depicted in Fig. 5.31. This behavior represents a highly complex array of operating modes that vastly enhance mode competition within the device. The RPM-12a, with PoP extractor, operated in the even π -mode (0.99 to 1.00 GHz) on approximately 40 % of the recorded shots for both the vertical and the horizontal configuration. The even π mode was excited using applied magnetic fields from 0.18 T to 0.26 T with pulsed voltages between -250 and -300 kV, which

despite the smaller AK gap with the MCC-2 (2.6 cm), were still less than the values predicted by the theoretical B-H model.

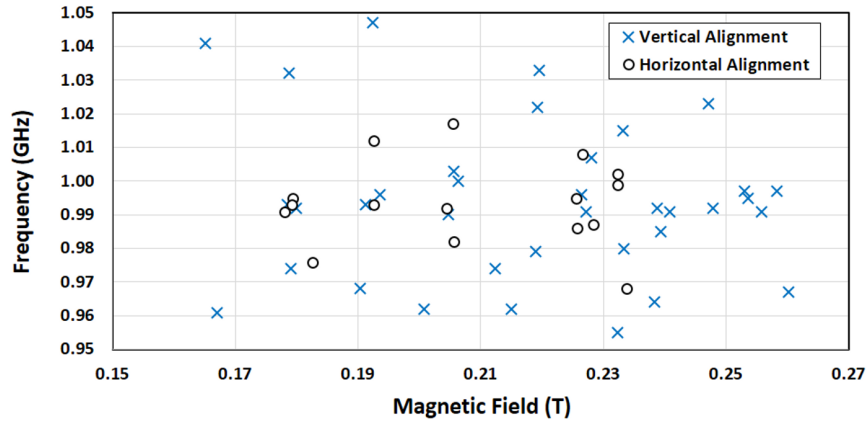


Figure 5.31. Dominant operating frequency observed in experimental runs of the RPM-12a with PoP extractor as a function of applied magnetic field for both the vertical (blue-X) and horizontal (black-O) configurations.

CHAPTER VI

Summary and Conclusions

6.1 Overview of the Recirculating Planar Magnetron

The recirculating planar magnetron (RPM), since its inception at the University of Michigan, has developed from a concept to a 150 MW, high-power, experimental source. Research and developmental work on this device has included analytic and theoretical design, feasibility and proof of principle simulations, prototyping and diagnostic development, experimental analysis, as well as several performance-enhancing inventions such as the mode control cathode (MCC) and coaxial extraction techniques.

Theoretical research on the device largely focused on the resonance and synchronism conditions for a planar slow-wave structure. Analytic theory described in Chapter 2 provides the basis for designing the resonant planar cavity array by relating resonant frequency, RF circuit phase velocity, and the applied crossed-field configuration (required to synchronously drive an electron beam); this led to simplified periodic dimensions of the device. Techniques for improving mode separation using the MCC geometry were also presented and showed that with sufficient proximity to the resonant cathode, the MCC could realistically provide as much as 10% mode separation between even and odd modes. The analytic theorem for the resonant structure of

the MCC can also be applied to other similar, but distinctly different devices, such as a periodic “shaped” cathode and a dual cavity structure, (whereby both the cathode and anode house resonant cavities)[88]. The odd-mode solution of the MCC resonance condition shares the same boundary conditions as either of these devices and, for this particular set of modes, is not exclusively limited to the assumption of symmetry about the horizontal axis of the device.

6.1.1 Numerical Summary

The numerical research on the RPM was focused primarily on the RPM-12a, a 1 GHz, 12-cavity prototype. Evaluation of the device was subdivided into cathode categories which included the solid cathode, LC-1, the proof-of-principle MCC, and the two experimental variants MCC-1 and MCC-2.

The dispersion relation and B-H condition for the RPM were numerically validated in simulation using the finite element solver HFSS as well as the particle-in-cell codes MAGIC. The 2D analytic dispersion matched the periodic simulated model to within 1-2 %, with error being attributed to acceptable convergence criteria and the inclusion of fringing RF fields at the corners of each cavity (which have been shown to induce up to 3% difference in resonant frequency)[89]. Fully 3D, finite cavity models suggests that the resonant frequency for all modes decreases. Modes that share the same periodicity as the planar cavity array such as π -mode are less affected by the finite length of the anode, whereas neighboring $5\pi/6$ and $7\pi/6$ -modes are heavily shifted, resulting in substantially increased mode separation than analytically predicted. The RPM-12a geometry, which for an infinite planar cavity array has an even- π mode at 1.02 GHz and an even $5\pi/6$ -mode at 1.014 GHz, was shown to resonate at 1.011 GHz and 0.989 GHz respectively for the 3D finite cavity array. The 22 MHz mode

separation (between the even π and even $5\pi/6$ modes) of the 3D simulation is nearly four times that predicted by the 2D infinite array.

Fully 3D particle-in-cell simulations were used to validate the analytic and numerical dispersion relations as well as the beam-wave synchronism conditions described by the Buneman-Hartree relation. Simulated models of the solid LC-1 cathode deviated from classical B-H theory, and operated in π modes at applied magnetic fields that were up to 30% higher than analytically predicted. This discrepancy is due to the formation of the electron hub above the cathode surface (virtual cathode effect). This effect can be compensated for by reducing the AK gap, used in the analytical calculation, to the distance from the virtual cathode to the anode rather than the cathode surface to the anode. The MCC-1 displayed much stronger agreement with B-H theory as the electron hub was able to form within the slots of the cathode and prevent the cathode surface from becoming electrostatically shielded. Simulations of the MCC-1 readily demonstrated phase-locking between the two RPM oscillators which occurred 55-75 ns after the startup. The MCC-2, which reduced the AK gap of the RPM-12a from 3.38 cm with the MCC-1 to 2.6 cm, achieved locked operation in 30 ns post-startup when operating in the even π mode and 48 ns when operating in the odd π -mode. No odd π mode operating states were observed when using the MCC-1 during the study.

6.1.2 Experimental

Experimental studies were performed to validate the dispersion relation and determine the feasibility of locking the RPM oscillators using the LC-1, MCC-1, and MCC-2 cathodes. Each cathode in the RPM produced high power microwave (HPM) pulses for durations of 50-300 ns in the vicinity of even- π mode ~ 1.01 GHz. Due to excessive current emission for small AK gaps, magnetic fields theoretically required

to attain synchronism were not achievable in experiment. Microwave oscillations typically developed in the RPM-12a as the effective AK gap was reduced due to plasma expansion and gap closure, thereby increasing beam velocity until synchronism was achieved. As a result of this limitation, consistently targeting a single mode of operation was not possible.

The LC-1, despite limited means of cross-oscillator communication, demonstrated brief periods of phase-locking based on the ± 10 and ± 15 degree criteria with average durations of 26 ns and 35 ns respectfully. Each MCC-1 model: MCC-1, MCC-1L, and MCC-1Lg achieved similar durations of locked operation with varying degrees of consistency. The MCC-1 reached a ± 10 degree locked state of operation in 60 % of shots, in which both oscillators were operational for 100 ns or more, as compared to 23 % using the LC-1. The MCC-1L and MCC-1Lg, both of which featured an axially lengthened conductor array, displayed reduced consistency in reaching the same locked state (25%, 17% respectfully). The MCC-1L and MCC-1Lg, however, demonstrated much faster startup times, upwards of 400 ns before the startup using the LC-1.

Microwave power extraction was designed in a two stage process which featured the proof of principle (PoP), vane antenna model, and the coaxial-all-cavity-extractor (CACE). The PoP was installed on the RPM-12a with MCC-2 and operated with 0.15 to 0.24 T axial magnetic fields and -250 to -300 kV applied voltage. Operating frequencies for this stage of experiment were predominantly observed between 0.97 and 1.01 GHz, which define the boundaries between the odd $5\pi/6$ and even π -modes. Microwave power measurements, made using a directional loop coupler, recorded peak extracted powers between 20-175 MW for durations of 50 to 100 ns. Despite these high peak fields at ~ 1 GHz, no breakdown was observed in the DFA-

650c coupler or the 74 ohm coaxial transmission line.

6.1.3 RPM-340 CACE design

The RPM-340 CACE is a 12-cavity, 1.9 GHz oscillator design which features an efficient, high power, extraction mechanism based on the “All Cavity Extractor” as well as many improvements derived from the operation of the RPM-12a such as the MCC. Using ICEPIC, numerical optimizations of this model were performed which resulted in improved efficiency (50-60 %) and extracted power (400-600 MW) in simulation. Based on the results of this study, a full scale prototype of the device is being developed for experimental use at the University of Michigan (see Appendix B). Similar to the PoP extractor, the RPM-CACE will use the same coaxial transmission line design and utilized a more complex coaxial-to-waveguide coupler that is designed for higher power handling, the DFA-340e. Despite simulated results suggesting that the RPM-CACE will produce ten times the total output power of the PoP extractor, the peak electric field at any given position in the device is anticipated to be of the same order of magnitude. The output power is split into six output waveguides instead of two and the electric field reduction in the DFA-340e, as compared to the DFA-650c, is expected to compensate for the increased power per waveguide.

The RPM-CACE is a novel approach to realizing a highly compact RF source whose high efficiency operation, reduced magnetic field volume, and axially oriented waveguide extraction scheme make it ideal for deployment onto vehicles and aircraft. Experiments performed on the RPM-12a suggest that despite favorable simulation results, mode competition and subsequent pulse shortening may still be present during the experimental operation of the RPM-CACE, but should not preclude the device from achieving high peak powers and efficiency. Suppression of these deleterious phenomena may be gained by adapting mode separation and priming techniques

which have been classically used on relativistic cylindrical magnetrons. Appendix (C) depicts several of these planar adaptations including, a 70 % efficient “rising sun” RPM, as well as magnetically and electrically primed mode control cathodes. The RPM has seen significant advancement over the past five years and continues to demonstrate, in both simulation and experiment, the capability to expand the operating parameters of relativistic magnetrons.

APPENDICES

APPENDIX A

Schematics for the RPM-12a and Cathodes

Schematic drawings for the RPM-12a (Fig. A.1), LC-1 (Fig. A.2(A-B)), MCC-1 (Fig. A.3(A-C)), and MCC-2 (Fig. A.4(A-C)) featuring useful dimensions in centimeters. The MCC-1 dimensions reflect the initial prototype, which constrains approximately 15 cm between the cylindrical endhats. The MCC-1L and MCC-1Lg, described in chapters 3-6, allow for 20 cm separation between endhats but is otherwise identical to the drawings in Fig. A.3.

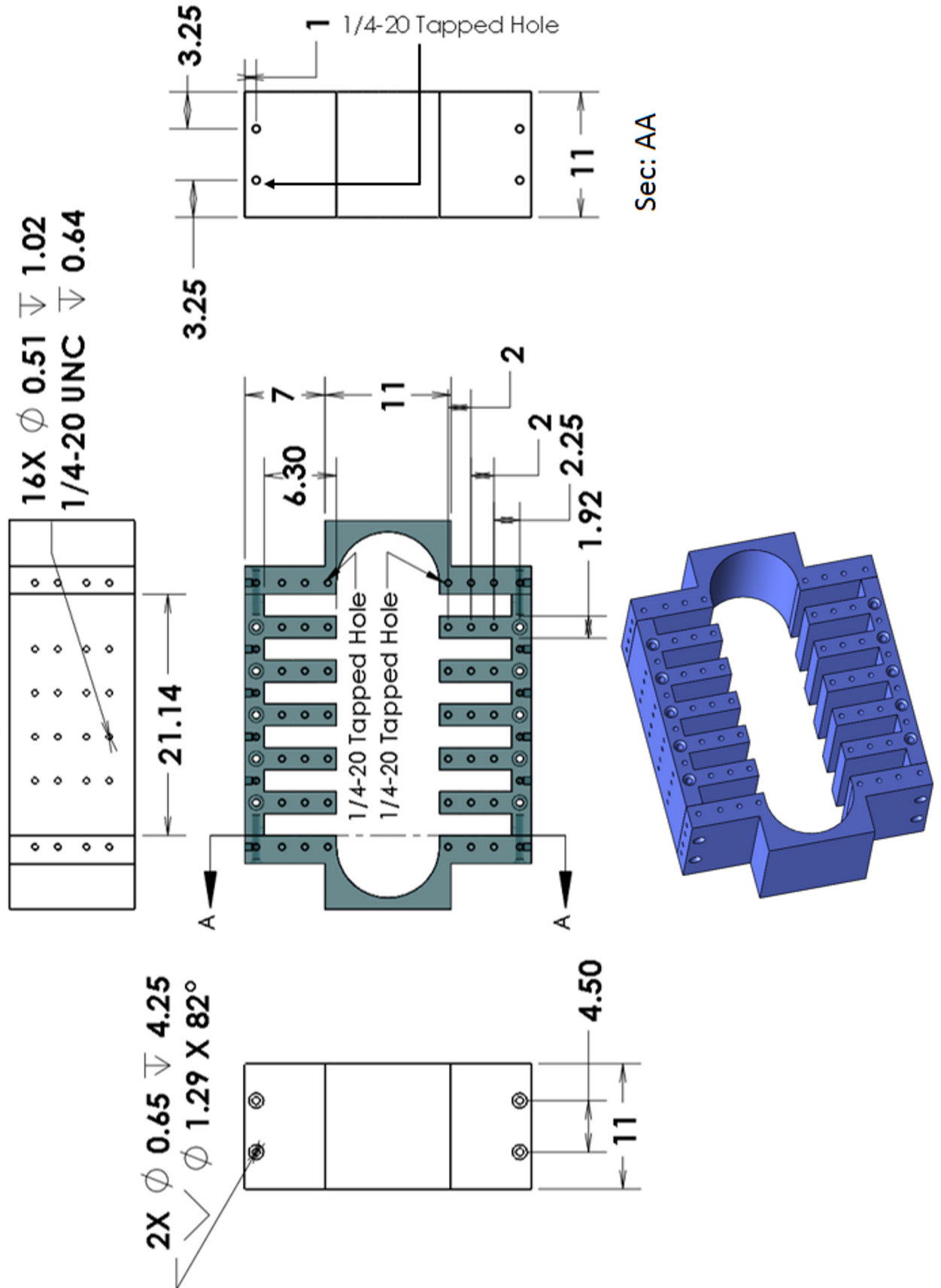
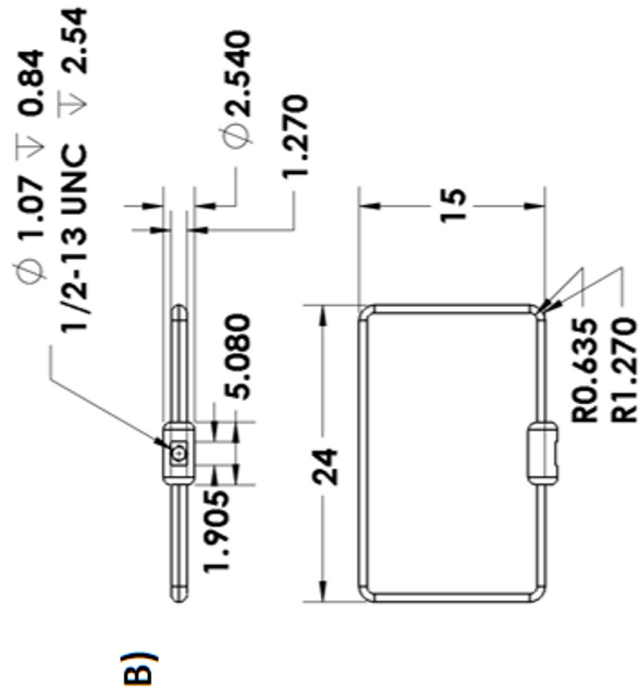
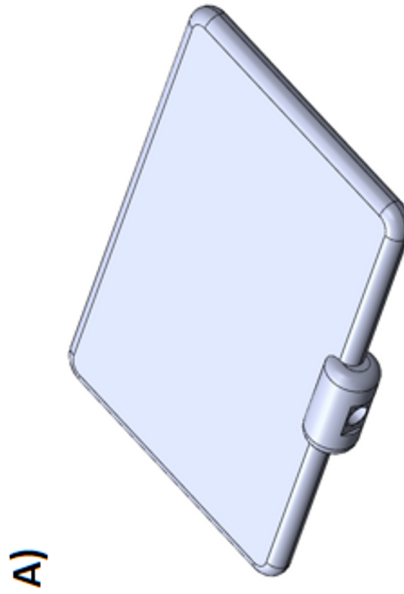


Figure A.1. Experimental schematic drawings of the RPM-12a (cm).



B)



A)

Figure A.2. Experimental schematics for the LC-1 solid cathode include: A) 3D-Solidworks rendering, and B) dimensions of the LC-1 (cm).

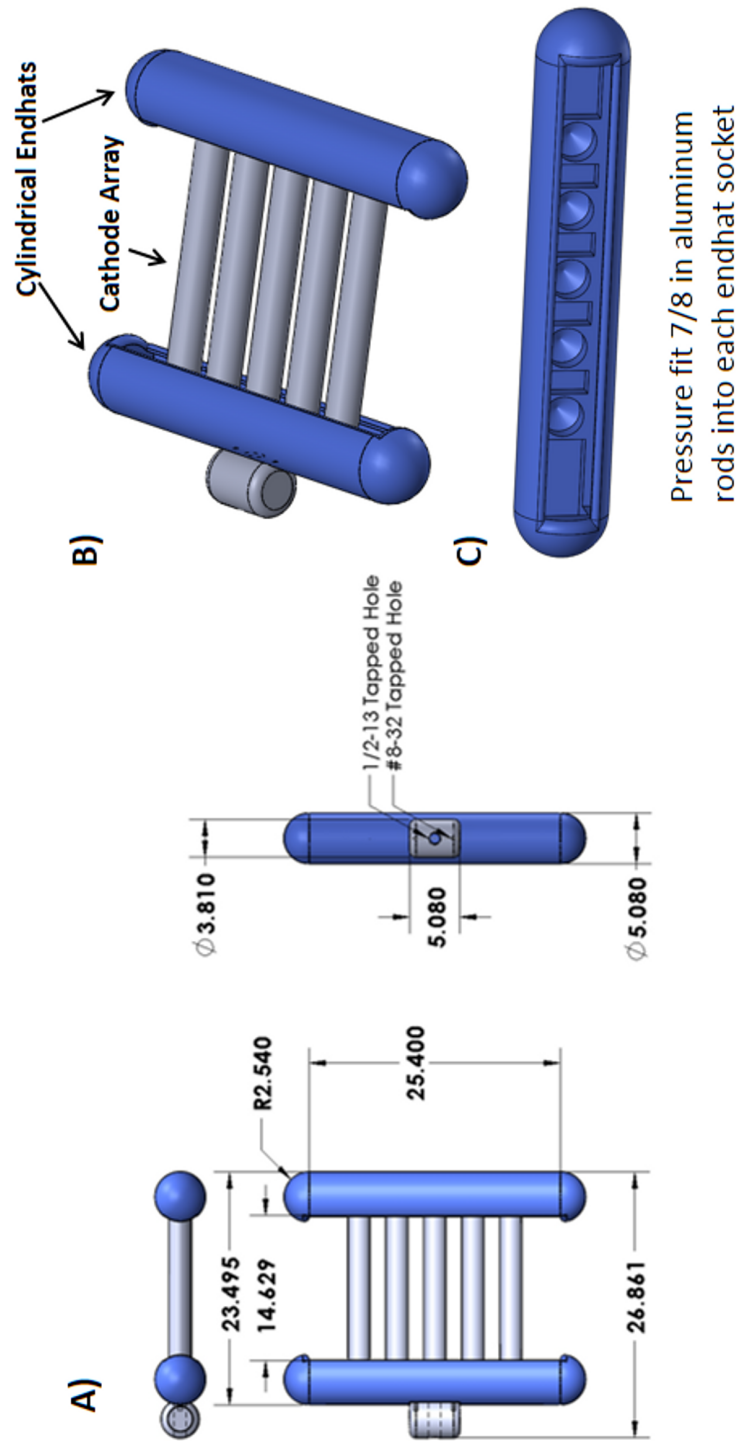


Figure A.3. Experimental schematics of the MCC-1 including: A) primary dimensions of the MCC-1 (cm), B) 3D Solidworks rendering of the MCC-1, and C) 3D Solidworks rendering of a single MCC endhat.

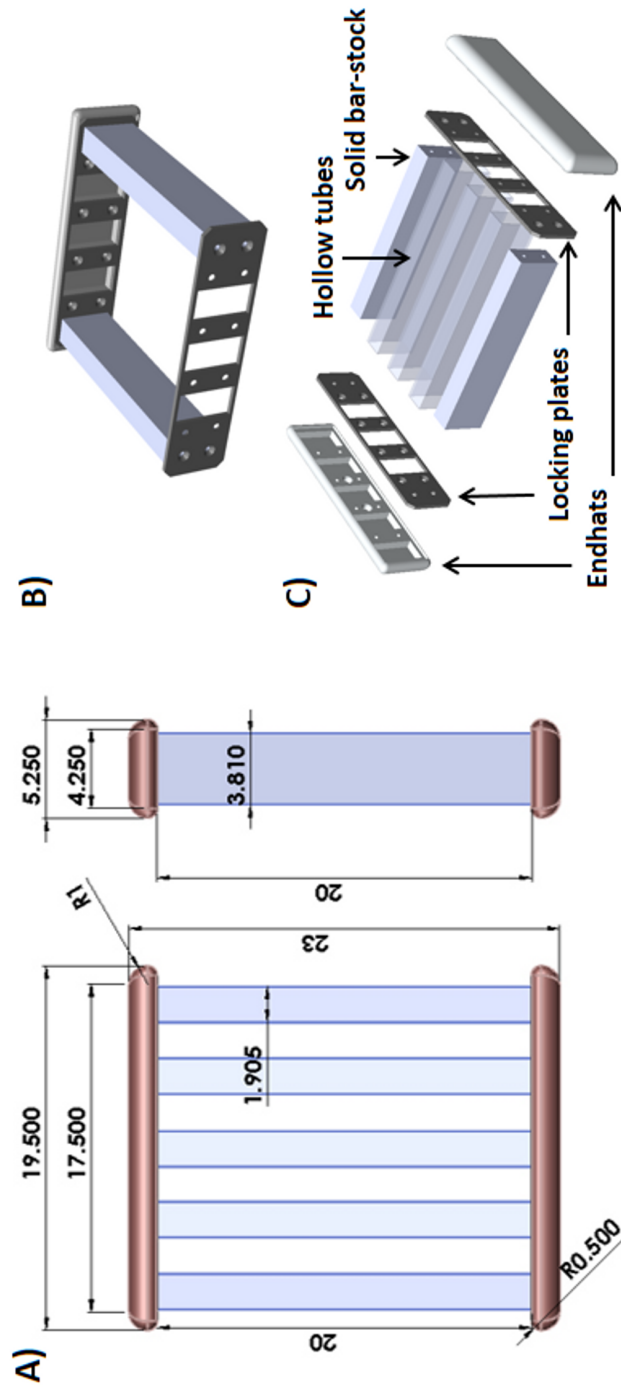


Figure A.4. Experimental schematic of the MCC-2 including: A) primary dimensions of the MCC-2 (cm), B) 3D Solidworks rendering of a partially assembled MCC-2, and C) 3D Solidworks rendering of the MCC-2 (exploded perspective).

APPENDIX B

RPM-340 CACE Schematics

The RPM-340 CACE experiment features twelve resonant cavities which couple into six output coaxial transmission lines (three on each oscillator), illustrated in Fig. B.1A. Each transmission line is converted to WR-340 rectangular waveguide (Fig. B.1B), axially downstream from the RPM, using DFA-340e (not shown). Diagnostic access to each output waveguide is provided using a 45 degree bend on the two exterior waveguide sections on either oscillator, shown in Fig. B1c. Schematic drawings are provided for the RPM-340 anode (Fig. B2) and the MCC-3 (Fig. B3(A-C)) which are featured in the RPM-340 CACE series of experiments. Axial cross section (XZ), graphically rendered in Fig. B4(A-B), provide a detailed labels of the components comprising the RPM-340 CACE assembly. An experimental photograph of the RPM-340 anode (pre-brazing) is shown in Fig. B5.

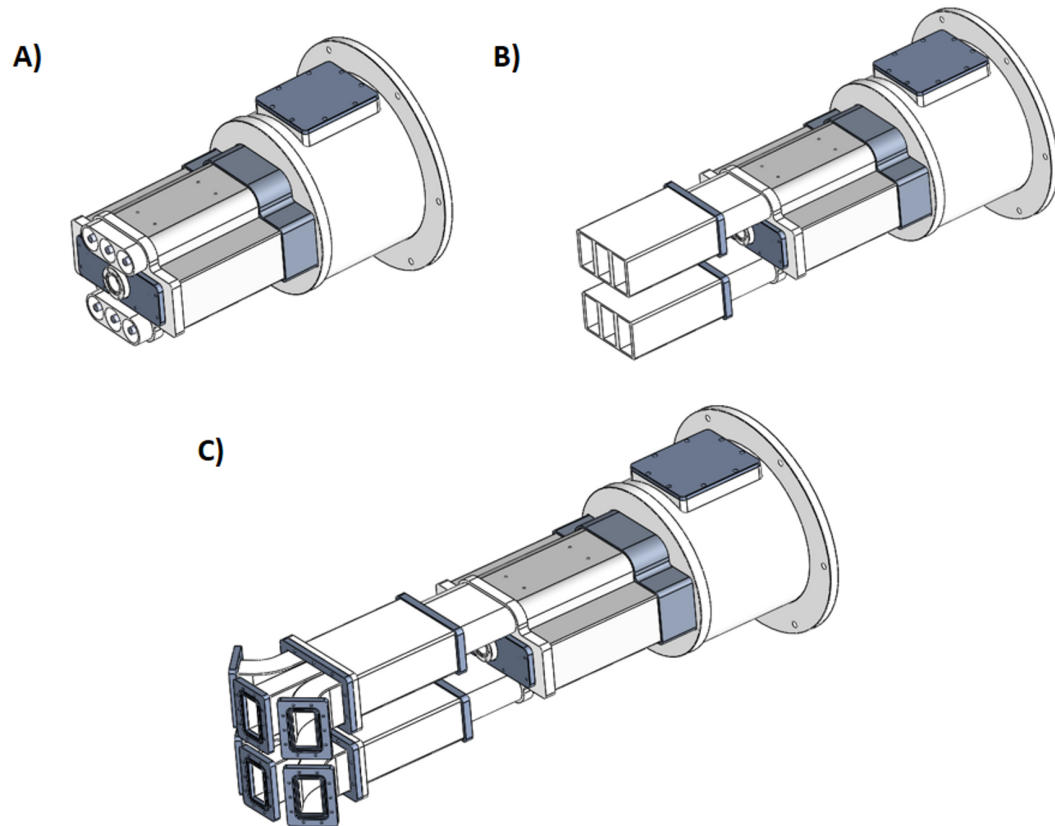


Figure B.1. RPM-340CACE with: A) Main body up through the coaxial transmission lines, and B) main body up through WR340 waveguide and C) Complete RPM-340 CACE assembly.

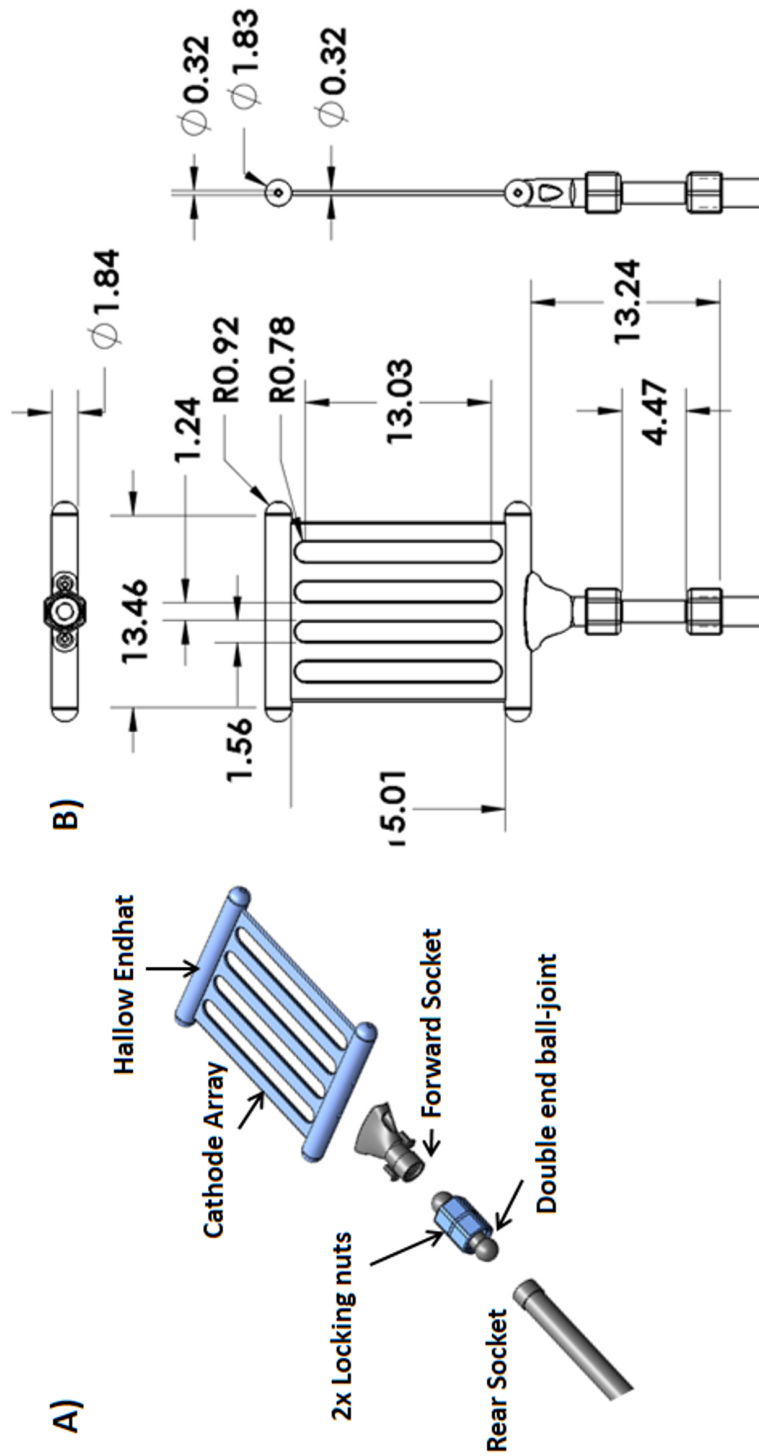


Figure B.3. Experimental schematic of the MCC-3 including: A) 3D Solidworks rendering of the MCC-3 (exploded perspective), and B) primary dimensions of the MCC-3 (cm).

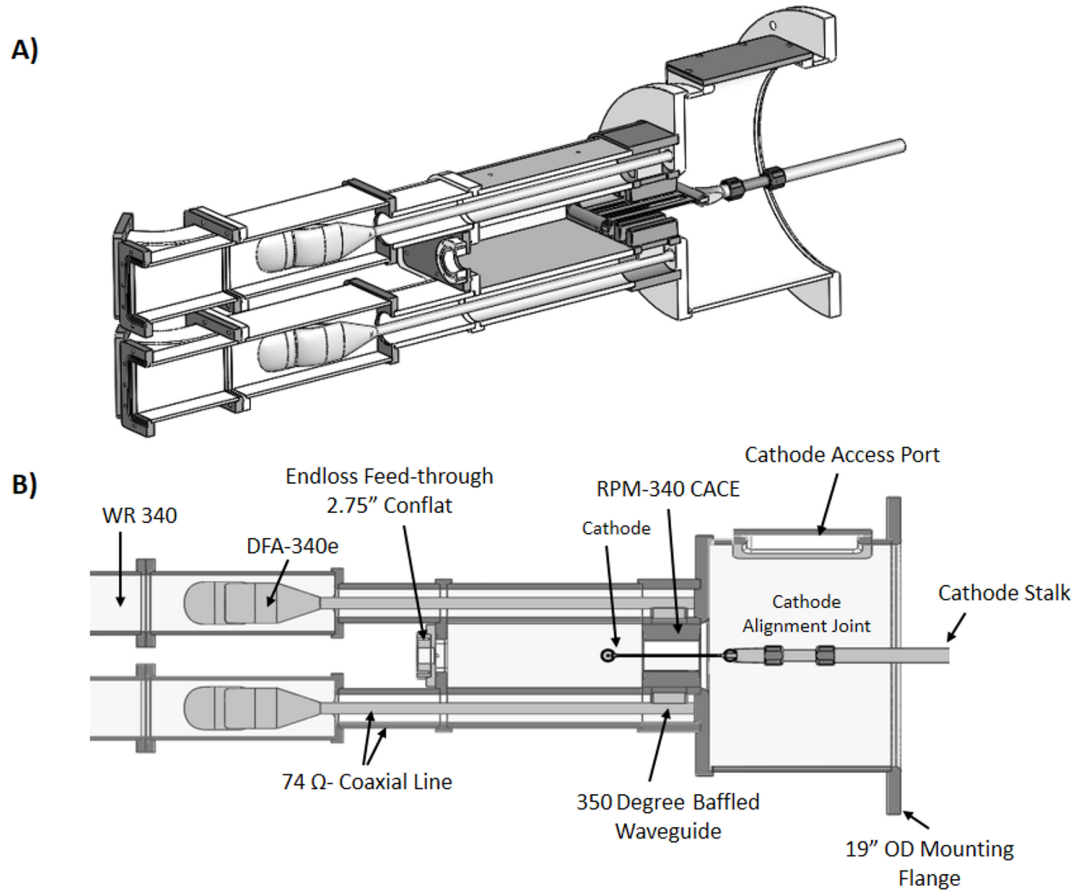


Figure B.4. A) Oblique 3D cross-section of the RPM CACE, and B) 2D longitudinal (XZ) cross-section of the RPM CACE.

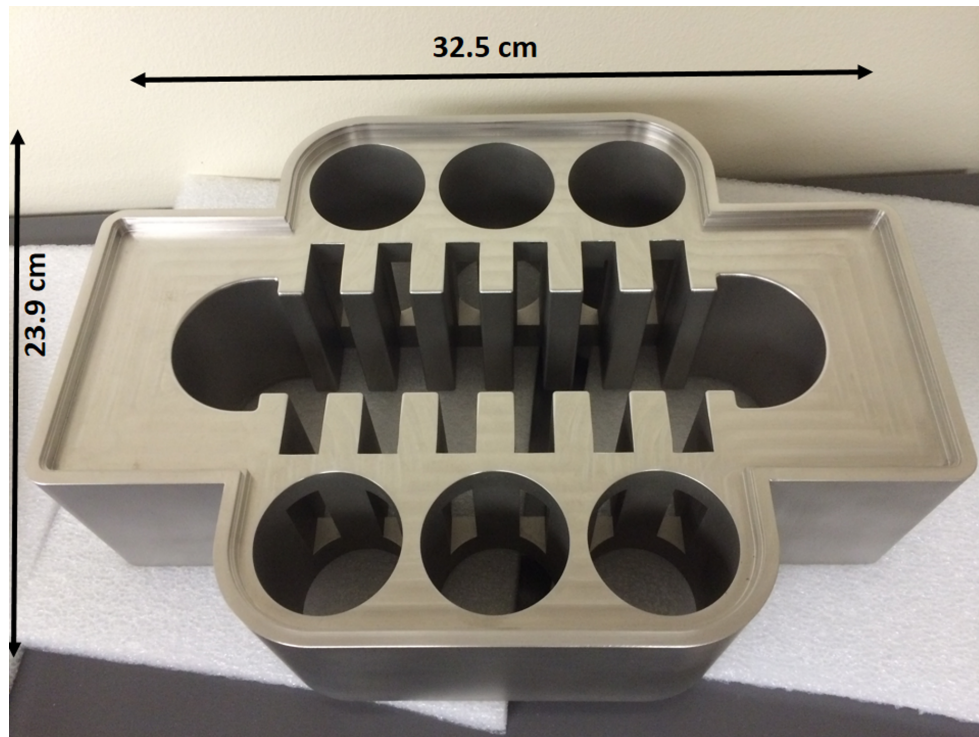


Figure B.5. Experimental photo of RPM-340 CACE Anode (Pre-assembly)

APPENDIX C

Planar Adaptations of Cylindrical Magnetron Concepts

Several techniques, classically used to improve the operation of cylindrical magnetron, were adapted for conceptual implementation on the planar cavity arrays of the RPM. These features include, rising sun resonant structures (Fig. C1(A-B)), magnetic cathode priming (Fig. C2(1-2)), and electric cathode priming (Fig. C3). The rising sun magnetron, shown operating in the even π -mode at 0.95 GHz in Fig. C1a, was designed to keep the length of the cavities (h) the same, but alter their resonant frequency (f_0) by increasing the width (w_1) in every other cavity (consistent with the rising sun configuration). Keeping the length of each cavity equal allows for the use of the CACE extractor, which provides a compact and efficient means of extracting microwave power. According to Fig. C1b, this L-band model was simulated to produce up to 1.3 GW output power with efficiencies between 60-70 percent.

The periodicity of the conducting array of the MCC lends itself well to priming π mode operation. The structure, which inherently provides emission priming, can be manipulated by adjusted the size and alignment of the conducting array to generate periodically varying magnetic (Fig. C2) or electric field (Fig. C3) with a wavelength equal to the guided wavelength of π -mode.

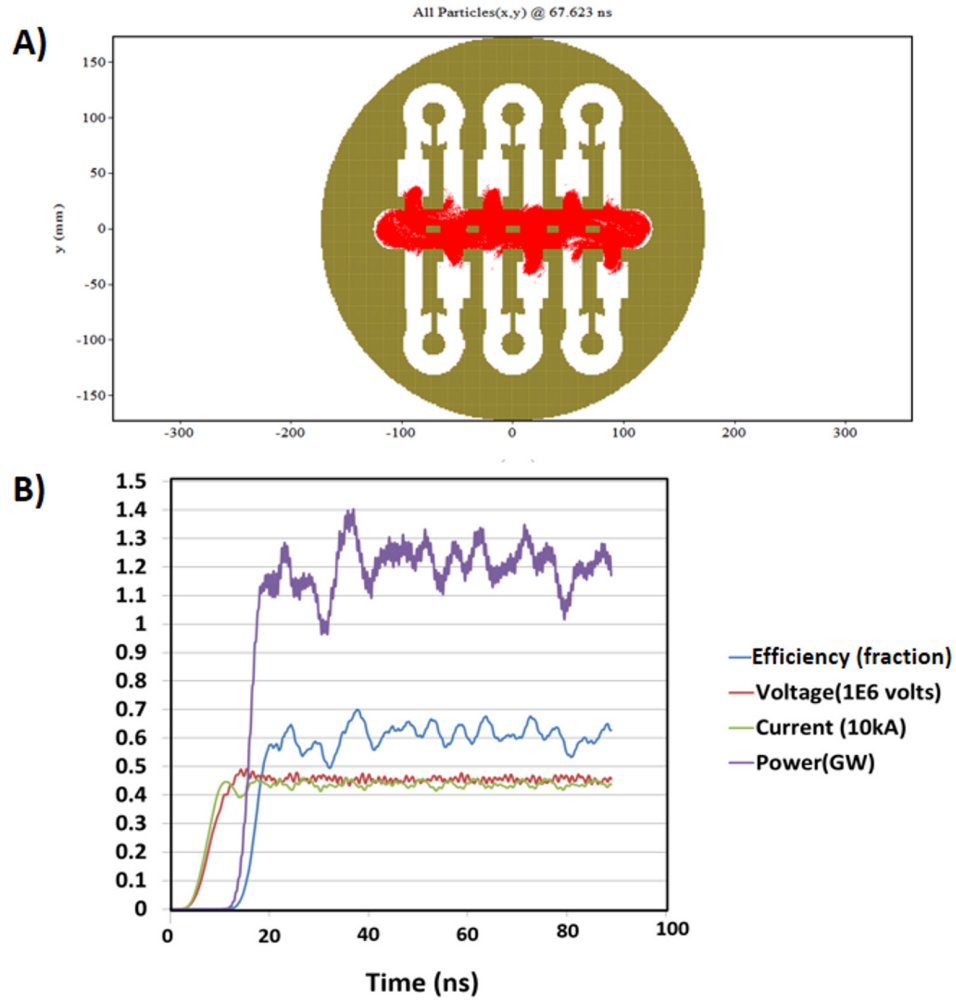


Figure C.1. A) Transverse (XY) cross section of a planar, rising sun, variant operating in π -mode that includes the MCC and CACE system, and B) simulated shot profile showing voltage, current, power and efficiency as a function of time.

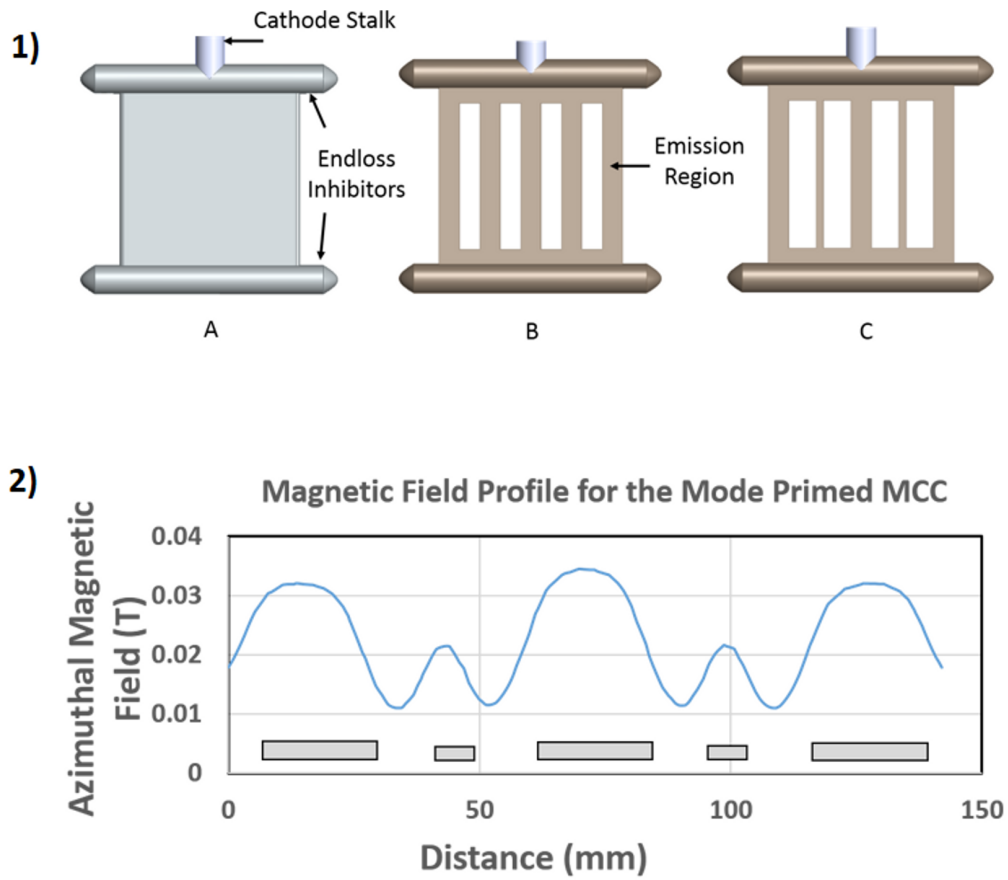


Figure C.2. 1) Top-down perspective of: a) solid cathode, b) standard MCC, and c) a magnetically primed MCC; 2) magnetic field profile on the surface of the cathode due to axial current of 1 kA.

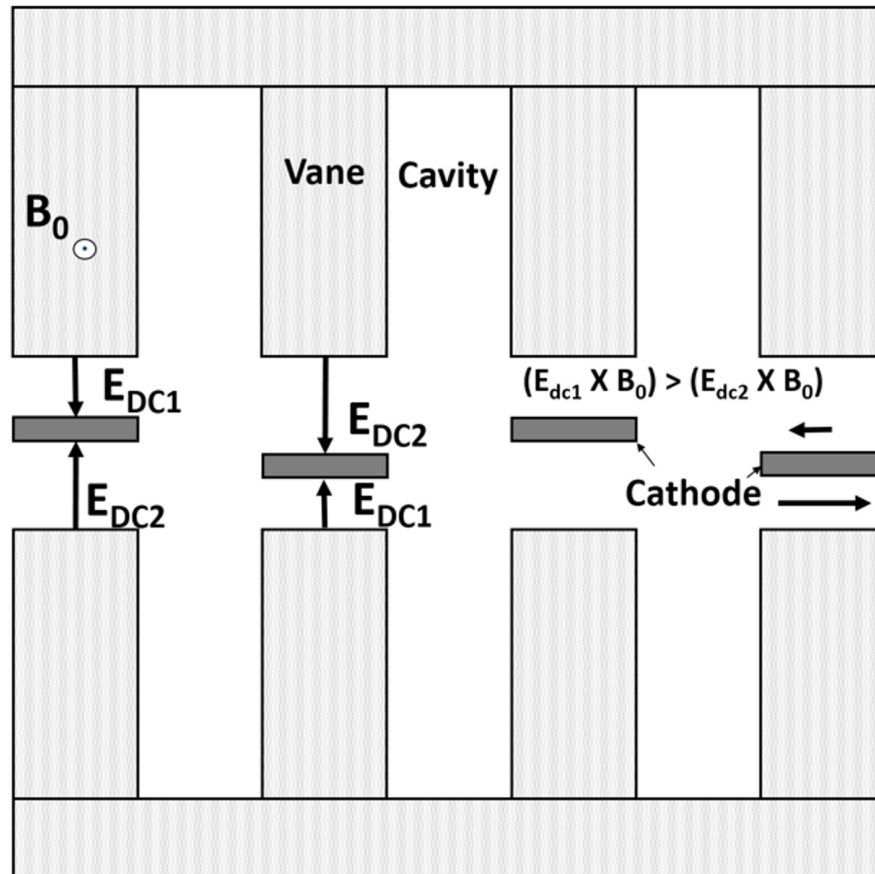


Figure C.3. Transverse (XY) cross section of the electrically primed MCC.

Bibliography

- [1] R.M. Gilgenbach, Y.Y. Lau, H. McDowell, and K.L. Cartwright, "*Crossed-Field Devices*": *Modern microwave and millimeter-wave power electronics* (Robert J. Barker, Neville C. Luhmann, John H. Booske, and Gregory S. Nusinovich, eds). Piscataway, NJ: Wiley-IEEE Press, Apr. 2005.
- [2] Y. Y. Lau, *Theory of Cross Field Devices and a Comparative Study of Other Radiation Sources: High Power Microwave Sources* (V.L. Granatstein and I. Alexeff, eds.). Artech House, July 1987.
- [3] G. B. Collins, *Microwave magnetrons*, vol. 6. McGraw-Hill New York, 1948.
- [4] A. S. Gilmour, *Klystrons, Traveling Wave Tubes, Magnetrons, Crossed-Field Amplifiers, and Gyrotrons*. Artech House, 2011.
- [5] T. A. Spencer, "Current HPM Source Research," in *High Energy Density and High Power RF* (S. H. Gold and G. S. Nusinovich, eds.), vol. 691 of *American Institute of Physics Conference Series*, pp. 46–46, Dec. 2003.
- [6] J. Benford, J. A. Swegle, and E. Schamiloglu, *High Power Microwaves, Second Edition*. CRC Press, Feb. 2007.
- [7] J. Benford, "History and future of the relativistic magnetron," in *Origins and Evolution of the Cavity Magnetron (CAVMAG), 2010 International Conference on the*, pp. 40–45, Apr. 2010.

- [8] R. Lemke, T. Genoni, and T. Spencer, “Effects that limit efficiency in relativistic magnetrons,” *IEEE Transactions on Plasma Science*, vol. 28, pp. 887–897, June 2000.
- [9] M. Fuks and E. Schamiloglu, “70% efficient relativistic magnetron with axial extraction of radiation through a horn antenna,” *IEEE Transactions on Plasma Science*, vol. 38, pp. 1302–1312, June 2010.
- [10] A. Palevsky and G. Bekefi, “Microwave emission from pulsed, relativistic e-beam diodes. II - the multiresonator magnetron,” *Physics of Fluids*, vol. 22, pp. 986–996, 1979.
- [11] M.C. Jones, V. B. Neculaes, Y.Y. Lau, R.M. Gilgenbach, and W.M. White, “Cathode priming of a relativistic magnetron,” *Applied Physics Letters*, vol. 85, pp. 6332–6334, Dec. 2004.
- [12] M. C. Jones, *Cathode priming of a relativistic magnetron using multi-emission zones on projection ablation lithography cathodes*. PhD thesis, University of Michigan, 2005.
- [13] V. B. Neculaes, R. M. Gilgenbach, and Y. Y. Lau, “Low-noise microwave magnetrons by azimuthally varying axial magnetic field,” *Applied Physics Letters*, vol. 83, pp. 1938–1940, Sept. 2003.
- [14] B.W. Hoff, R.M. Gilgenbach, N.M. Jordan, Y.Y. Lau, E.J. Cruz, D.M. French, M.R. Gomez, J.C. Zier, T.A. Spencer, and D. Price, “Magnetic priming at the cathode of a relativistic magnetron,” *IEEE Transactions on Plasma Science*, vol. 36, pp. 710–717, June 2008.
- [15] V. B. Bogdan Neculaes, M. C. Jones, R. Gilgenbach, Y. Y. Lau, J. Luginsland,

- B. Hoff, W. White, N. Jordan, P. Pengvanich, Y. Hidaka, and H. Bosman, "Magnetic priming effects on noise, startup, and mode competition in magnetrons," *IEEE Transactions on Plasma Science*, vol. 33, pp. 94–102, Feb. 2005.
- [16] V. Bogdan Neculaes, R. Gilgenbach, Y. Y. Lau, M. C. Jones, and W. White, "Low-noise microwave oven magnetrons with fast start-oscillation by azimuthally varying axial magnetic fields," *IEEE Transactions on Plasma Science*, vol. 32, pp. 1152–1159, June 2004.
- [17] V. B. Neculaes, R. M. Gilgenbach, and Y.-Y. Lau, "Low noise, crossed field devices such as a microwave magnetron, microwave oven utilizing same and method of converting a noisy magnetron to a low-noise magnetron," Mar. 2005. US Patent Number: US6872929 B2.
- [18] W. White, R. Gilgenbach, M. C. Jones, V. Bogdan Neculaes, Y.-Y. Lau, P. Pengvanich, N. Jordan, B. Hoff, R. Edgar, T. Spencer, and D. Price, "Radio frequency priming of a long-pulse relativistic magnetron," *IEEE Transactions on Plasma Science*, vol. 34, pp. 627–634, June 2006.
- [19] J. Kim, J. Won, G.-S. Park, H. Ha, and J. Shon, "Reduction of noise in strapped magnetron by electric priming using anode shape modification," in *Vacuum Electronics Conference, 2006 held Jointly with 2006 IEEE International Vacuum Electron Sources., IEEE International*, pp. 355–356, 2006.
- [20] K. Cartwright, P. Mardahl, M. D. Haworth, V. B. Neculaes, M. Jones, M. Lopez, Y. Lau, and R. Gilgenbach, "Simulation of a relativistic magnetron with a varying axial magnetic field," in *The 31st IEEE International Conference on Plasma Science, 2004. ICOPS 2004. IEEE Conference Record - Abstracts*, pp. 275–, July 2004.

- [21] Y. Y. Lau, "Simple theory for the two-dimensional Child-Langmuir law," *Physical Review Letters*, vol. 87, p. 278301, Dec. 2001.
- [22] J. Hull, "Inverted magnetron," *Proceedings of the IRE*, vol. 40, pp. 1038–1041, Sept. 1952.
- [23] R.M. Gilgenbach, Y.Y. Lau, D. M. French, B. W. Hoff, J. Luginsland, and M.A. Franzi, "Crossed field device," Aug. 2010. US Patent Number: US-20110204785-A1 (Patent pending).
- [24] R. Gilgenbach, Y. Y. Lau, D. French, B. Hoff, M. Franzi, and J. Luginsland, "Recirculating planar magnetrons for high-power high-frequency radiation generation," *IEEE Transactions on Plasma Science*, vol. 39, pp. 980–987, Apr. 2011.
- [25] W. C. Brown, "Traveling wave device," Feb. 1967. US Patent Number: US3305751A.
- [26] P. L. Kapitza and L. A. Wainstein, *High-power Electronics: Ed. by P. L. Kapitza and L.A. Wainstein ; Transl. from the Russian by S. and M. Nikolic. High-power microwave electronics*, vol. 1. Pergamon Press, 1964.
- [27] L. Ludeking, G. E. Thomas, and W. Bollen, "Simulation and analysis of a reentrant planar magnetron," in *Electron Devices Meeting, 1987 International*, vol. 33, pp. 160–163, 1987.
- [28] J.-I. Kim, S.-G. Jeon, Y.-S. Jin, G.-J. Kim, D.-H. Kim, and S.-S. Jung, "Particle-in-cell simulation of 100 GHz reentrant linear magnetron," in *33rd International Conference on Infrared, Millimeter and Terahertz Waves, 2008. IRMMW-THz 2008*, pp. 1–2, Sept. 2008.

- [29] J.-I. Kim, S.-G. Jeon, Y.-S. Jin, G.-J. Kim, D.-H. Kim, and S.-S. Jung, “Investigation of the 100GHz reentrant linear magnetron using particle-in-cell simulation,” *Journal of Vacuum Science & Technology B*, vol. 27, pp. 687–691, Mar. 2009.
- [30] R. V. Harrowell, “A new, radial b-field magnetron for use in microwave ovens,” *Journal of Physics D: Applied Physics*, vol. 17, pp. L43–L46, Mar. 1984.
- [31] M. A. Franzi, R. M. Gilgenbach, B. W. Hoff, D. A. Chalenski, D. Simon, Y. Y. Lau, and J. Luginsland, “Recirculating-planar-magnetron simulations and experiment,” *IEEE Transactions on Plasma Science*, vol. 41, pp. 639–645, Apr. 2013.
- [32] M. Franzi, R. Gilgenbach, Y. Y. Lau, B. Hoff, G. Greening, and P. Zhang, “Passive mode control in the recirculating planar magnetron,” *Physics of Plasmas*, vol. 20, p. 033108, Mar. 2013.
- [33] P. E. Volz and P. E. Volz, “Magnetron strapping for high power,” Jan. 1957. US Patent Number: US2777090.
- [34] S. Millman and A. T. Nordsieck, “The rising sun magnetron,” *Journal of Applied Physics*, vol. 19, pp. 156–165, Apr. 1948.
- [35] T. Treado, W. Doggett, G. Thomas, I. Smith, R.S., J. Jackson-Ford, and D. Jenkins, “Operating modes of relativistic rising-sun and a6 magnetrons,” *IEEE Transactions on Plasma Science*, vol. 16, pp. 237–248, Apr. 1988.
- [36] N. M. Kroll and W. E. Lamb, “The resonant modes of the rising sun and other unstrapped magnetron anode blocks,” *Journal of Applied Physics*, vol. 19, pp. 166–186, Apr. 1948.

- [37] A. V. Hollenberg, N. Kroll, and S. Millman, “Rising sun magnetrons with large numbers of cavities,” *Journal of Applied Physics*, vol. 19, pp. 624–635, Apr. 1948.
- [38] F. F. Chen, *Introduction to Plasma Physics and Controlled Fusion*. Springer, Jan. 1984.
- [39] L. Brillouin, “A theorem of larmor and its importance for electrons in magnetic fields,” *Physical Review*, vol. 67, pp. 260–266, Apr. 1945.
- [40] R. C. Davidson, G. L. Johnston, K. T. Tsang, and A. T. Drobot, “Cylindrical Brillouin flow in relativistic smooth-bore magnetrons,” in *Microwave and Particle Beam Sources and Directed Energy Concepts* (H. E. Brandt, ed.), vol. 1061 of *Society of Photo-Optical Instrumentation Engineers (SPIE) Conference Series*, pp. 186–200, July 1989.
- [41] J. C. Slater, *Microwave electronics*. Van Nostrand, 1950.
- [42] Y. Y. Lau, J. W. Luginsland, K. L. Cartwright, D. H. Simon, W. Tang, B. W. Hoff, and R. M. Gilgenbach, “A re-examination of the Buneman-Hartree condition in a cylindrical smooth-bore relativistic magnetron,” *Physics of Plasmas*, vol. 17, p. 033102, Mar. 2010.
- [43] R. V. Lovelace and T. F. T. Young, “Relativistic hartree condition for magnetrons: Theory and comparison with experiments,” *Physics of Fluids*, vol. 28, pp. 2450–2452, Aug. 1985.
- [44] E. Ott and R. Lovelace, “Magnetic insulation and microwave generation,” *Applied Physics Letters*, vol. 27, pp. 378–380, Oct. 1975.

- [45] D. H. Simon, Y. Y. Lau, J. W. Luginsland, and R. M. Gilgenbach, “An unnoticed property of the cylindrical relativistic brillouin flow,” *Physics of Plasmas*, vol. 19, p. 043103, Apr. 2012.
- [46] M. Fuks and E. Schamiloglu, “Rapid start of oscillations in a magnetron with a ”transparent” cathode,” *Physical review letters*, vol. 95, p. 205101, Nov. 2005. PMID: 16384067.
- [47] Y. Y. Lau and D. Chernin, “A review of the ac space charge effect in electron circuit interactions,” *Physics of Fluids: Plasma Physics*, vol. 4, pp. 3473–3497, Nov. 1992.
- [48] J. W. Gewartowski and H. A. Watson, *Principles of electron tubes: including grid-controlled tubes, microwave tubes, and gas tubes*. Van Nostrand, May 1965.
- [49] P. J. Christenson, D. P. Chernin, A. L. Garner, and Y. Y. Lau, “Resistive destabilization of cycloidal electron flow and universality of (near-) brillouin flow in a crossed-field gap,” *Physics of Plasmas*, vol. 3, no. 12, p. 4455, 1996.
- [50] J. Vaughan, “A model for calculation of magnetron performance,” *IEEE Transactions on Electron Devices*, vol. 20, pp. 818–826, Sept. 1973.
- [51] B. Goplen, L. Ludeking, D. Smith, and G. Warren, “User-configurable MAGIC for electromagnetic PIC calculations,” *Computer Physics Communications*, vol. 87, pp. 54–86, May 1995.
- [52] ANSYS, Inc., <http://www.ansys.com/Products/>, *High Frequency Structure Simulator*, v.15 ed.
- [53] T. P. Fleming, P. J. Mardahl, L. Bowers, and K. Cartwright, “Three dimensional PIC simulations of novel cathodes in the michigan and AFRL relativistic

- magnetrons,” in *Power Modulator Symposium, 2006. Conference Record of the 2006 Twenty-Seventh International*, pp. 401–404, May 2006.
- [54] Dassult Systems, <http://www.solidworks.com/sw/resources.htm>, *Solidworks 3D CAD software*, 2013 ed.
- [55] W. Woo, J. Benford, D. Fittinghoff, B. Harteneck, D. Price, R. Smith, and H. Sze, “Phase locking of high power microwave oscillators,” *Journal of Applied Physics*, vol. 65, pp. 861–866, Jan. 1989.
- [56] R. Adler, “A study of locking phenomena in oscillators,” *Proceedings of the IEEE*, vol. 61, pp. 1380–1385, Oct. 1973.
- [57] P. Pengvanich, Y. Y. Lau, E. Cruz, R. M. Gilgenbach, B. Hoff, and J. W. Luginsland, “Analysis of peer-to-peer locking of magnetrons,” *Physics of Plasmas*, vol. 15, p. 103104, Oct. 2008.
- [58] J. Borghetti, “Waveguide to coaxial transition having the coaxial outer conductor extending into the waveguide,” May 1965. US Patent Number: US3182272A.
- [59] W. W. Mumford, “Broad band coaxial line to wave guide coupler,” Oct. 1950. US Patent Number: US2527146 A.
- [60] J. Borghetti, “Inline waveguide to coaxial transition,” Feb. 1962. US Patent Number: US3023382 A.
- [61] R. Levy and L. Hendrick, “Analysis and synthesis of in-line coaxial-to-waveguide adapters,” in *Microwave Symposium Digest, 2002 IEEE MTT-S International*, vol. 2, pp. 809–811 vol.2, June 2002.
- [62] W. C. Brown and I. J. Myers, “Magnetron coaxial adaptor having a cap which

- fits over the magnetron output antenna,” June 1993. US Patent Number: US5216327A.
- [63] A. D. Greenwood, “All cavity magnetron axial extractor,” Sept. 2006. US Patent Number: US7106004 B1.
- [64] B. Hoff, A. Greenwood, P. Mardahl, and M. Haworth, “All cavity-magnetron axial extraction technique,” *IEEE Transactions on Plasma Science*, vol. 40, pp. 3046–3051, Nov. 2012.
- [65] B. W. Hoff, M. Franzi, D. M. French, G. Greening, and R. M. Gilgenbach, “A compact, pi-mode extraction scheme for the axial b-field recirculating planar magnetron,” Tech. Rep. AFRL-RD-PS-TR-2012-0039, Air Force Research Laboratory, July 2012.
- [66] P. Delmotte, “WAVEGUIDE-COAXIAL LINE TRANSITIONS,” 2001. Belgian Microwave Roundtable.
- [67] D. E. V. Clifton C. Courtney, “Modes of a double baffled, cylindrical, coaxial waveguide.” Sensor and Simulation Notes, August 2003. Note 483.
- [68] R. E. Peterkin and J. W. Luginsland, “A virtual prototyping environment for directed-energy concepts,” *Computing in Science & Engineering*, vol. 4, pp. 42–49, Apr. 2002.
- [69] D. M. Pozar, *Microwave engineering*. Wiley.com, 2009.
- [70] D. Price, J. Levine, and J. Benford, “Diode plasma effects on the microwave pulse length from relativistic magnetrons,” *IEEE Transactions on Plasma Science*, vol. 26, pp. 348–353, June 1998.

- [71] W. D. Kilpatrick, "Criterion for vacuum sparking designed to include both rf and dc," *Review of Scientific Instruments*, vol. 28, pp. 824–826, Oct. 1957.
- [72] T. P. Wangler, *RF Linear Accelerators*. John Wiley & Sons, Mar. 2008.
- [73] R. Woo, "RF voltage breakdown in coaxial transmission lines," *Proceedings of the IEEE*, vol. 57, pp. 254–256, Feb. 1969.
- [74] R. Lemke, T. Genoni, and T. Spencer, "Effects that limit efficiency in relativistic magnetrons," *IEEE Transactions on Plasma Science*, vol. 28, pp. 887–897, June 2000.
- [75] E. A. Abramyan, B. A. Altercop, and G. D. Kuleshov, "Microsecond intensive e-beams," in *1977 2nd International Topical Conference on Electron Beam Research Technology*, vol. 2, pp. 743–754, Oct. 1977.
- [76] M. R. Lopez, R. Gilgenbach, M. C. Jones, W. White, D. Jordan, M. Johnston, T. Strickler, V. Bogdan Neculaes, Y.-Y. Lau, T. Spencer, M. Haworth, K. Cartwright, P. Mardahl, J. Luginsland, and D. Price, "Relativistic magnetron driven by a microsecond e-beam accelerator with a ceramic insulator," *IEEE Transactions on Plasma Science*, vol. 32, pp. 1171–1180, June 2004.
- [77] R. K. Cacak and J. R. Craig, "Magnetic field uniformity around near helmholtz coil configurations," *Review of Scientific Instruments*, vol. 40, pp. 1468–1470, Nov. 1969.
- [78] M. Jones, V. B. Neculaes, Y. Lau, R. Gilgenbach, and W. White, "Cathode priming of a relativistic magnetron," *Applied Physics Letters*, vol. 85, pp. 6332–6334, Dec. 2004.

- [79] M. Fuks, N. Kovalev, A. Andreev, and E. Schamiloglu, "Mode conversion in a magnetron with axial extraction of radiation," *IEEE Transactions on Plasma Science*, vol. 34, pp. 620–626, June 2006.
- [80] N. F. Kovalev, B. D. Kolchugin, V. E. Nechaev, M. M. Ofitserov, E. I. Soluianov, and M. I. Fuks, "Relativistic magnetron with diffraction coupling," *Pisma v Zhurnal Tekhnicheskoi Fiziki*, vol. 3, pp. 1048–1052, Oct. 1977.
- [81] M. R. Lopez, R. M. Gilgenbach, Y. Y. Lau, D. W. Jordan, M. W. Johnston, M. C. Jones, V. B. Neculaes, T. A. Spencer, J. W. Luginsland, M. D. Haworth, R. W. Lemke, D. Price, and L. Ludeking, "Long-pulse relativistic magnetron experiments," in *Plasma Science - Abstracts, 2009. ICOPS 2009. IEEE International Conference on*, vol. 4720, pp. 10–17, 2002.
- [82] B. W. Hoff, *Magnetic priming of a relativistic magnetron*. PhD thesis, University of Michigan, 2009.
- [83] T. Smith, "Vector network analyzer techniques to measure wr340 waveguide windows," *Argonne National Laboratory Publication*, vol. Advanced Photon Source, pp. 1–5, June 2002.
- [84] T. Treado, I. Smith, R.S., C. Shaughnessy, and G. E. Thomas, "Temporal study of long-pulse relativistic magnetron operation," *IEEE Transactions on Plasma Science*, vol. 18, pp. 594–602, June 1990.
- [85] M. Haworth, J. Luginsland, and R. Lemke, "Evidence of a new pulse-shortening mechanism in a load-limited MILO," *IEEE Transactions on Plasma Science*, vol. 28, pp. 511–516, June 2000.
- [86] E. J. Cruz, B. W. Hoff, P. Pengvanich, Y. Y. Lau, R. M. Gilgenbach, and

- J. W. Luginsland, “Experiments on peer-to-peer locking of magnetrons,” *Applied Physics Letters*, vol. 95, p. 191503, Nov. 2009.
- [87] H. Sze, R. Smith, J. Benford, and B. Harteneck, “Phase-locking of strongly coupled relativistic magnetrons,” *IEEE Transactions on Electromagnetic Compatibility*, vol. 34, pp. 235–241, Aug. 1992.
- [88] G. Greening, M. A. Franzi, Y. Y. Lau, N. M. Jordan, and R. M. Gilgenbach, “Design of a prototype multi-frequency recirculating planar magnetron,” in *IEEE 41st International Conference on Plasma Science, 2014*, June 2014.
- [89] Y. Y. Lau and L. R. Barnett, “Theory of a low magnetic field gyrotron (gyromagnetron),” *International Journal of Infrared and Millimeter Waves*, vol. 3, pp. 619–644, Sept. 1982.